

A CO LINE AND INFRARED CONTINUUM STUDY OF THE ACTIVE STAR-FORMING COMPLEX W51

MIJU KANG^{1,2,3}, JOHN H. BIEGING³, CRAIG A. KULESA³, YOUNGUNG LEE¹, MINHO CHOI¹, AND WILLIAM L. PETERS³

Accepted for publication in ApJS

ABSTRACT

We present the results of an extensive observational study of the active star-forming complex W51 that was observed in the $J = 2 - 1$ transition of the ^{12}CO and ^{13}CO molecules over a $1^\circ 25' \times 1^\circ 00'$ region with the University of Arizona Heinrich Hertz Submillimeter Telescope. We use a statistical equilibrium code to estimate physical properties of the molecular gas. We compare the molecular cloud morphology with the distribution of infrared (IR) and radio continuum sources, and find associations between molecular clouds and young stellar objects (YSOs) listed in *Spitzer* IR catalogs. The ratios of CO lines associated with H II regions are different from the ratios outside the active star-forming regions. We present evidence of star formation triggered by the expansion of the H II regions and by cloud-cloud collisions. We estimate that about 1% of the cloud mass is currently in YSOs.

Subject headings: H II regions — stars: formation — ISM: individual (W51) — infrared: ISM — radio lines: ISM

1. INTRODUCTION

Establishing the properties of molecular clouds is essential in understanding the formation and evolution of star-forming regions. Newly formed massive stars can affect the parental molecular clouds through ionization, heating, and expansion of the H II regions, stellar winds, and supernova-driven shocks (Bieging et al. 2009; Beuther et al. 2007; Clark & Porter 2004; Gritschneider et al. 2009; Povich et al. 2009; Walborn et al. 2002). These mechanisms are either compressing or dispersing the surrounding clouds. For a better understanding of the feedback process in the interstellar medium (ISM), detailed observations of the molecular clouds and identification of embedded young stellar objects (YSOs) are required.

W51 is one of the most luminous star-forming regions in the first quadrant of the Galactic plane. The high luminosity comes from a large number of O-type stars (Bieging 1975; Mehringer 1994) that are within the molecular cloud (Mufson & Liszt 1979; Carpenter & Sanders 1998). In the 21 cm radio continuum map (Koo & Moon 1997), W51 can be divided into three regions: W51A (G49.4-0.3 and G49.5-0.4), W51B (G48.9-0.3, G49.0-0.3, G49.1-0.4, G49.10-0.27, G49.17-0.21, and G49.2-0.4), and W51C (Kundu & Velusamy 1967; Bieging 1975; Mufson & Liszt 1979; Koo & Moon 1997). While W51C shows a nonthermal continuum spectrum indicating a supernova remnant (Subrahmanyan & Goss 1995), W51A and W51B have thermal spectra indicating compact H II regions. The ionized gas in W51A is distributed in a broad velocity range of 40 to 80 km s⁻¹ (Crampton et al. 1978; Mehringer 1994; Pankonin et al. 1979; Wilson et al. 1970). The average systemic velocity of the ionized gas in W51B is ~ 66 km s⁻¹

(Downes et al. 1980; Pankonin et al. 1979; Wilson et al. 1970). In the Massachusetts-Stony Brook Galactic plane CO survey map covering the first Galactic quadrant (Sanders et al. 1986) the W51 region is distinguished by bright CO emission extending over a $1^\circ \times 1^\circ$ area centered on $(l, b) \sim (49^\circ 5', -0^\circ 2')$ at the velocity range from 45 to 75 km s⁻¹ (see Carpenter & Sanders 1998, Fig.1). Carpenter & Sanders (1998) studied this region in detail in the ^{12}CO and ^{13}CO $J = 1 - 0$ emission. They roughly divided the molecular clouds associated with the H II region complex into two groups: the W51 giant molecular cloud (GMC) and the 68 km s⁻¹ cloud. They calculated a virial mass of $1.2 \times 10^6 M_\odot$ in the W51 GMC and $1.9 \times 10^5 M_\odot$ in the 68 km s⁻¹ cloud. Because the maximum velocity permitted by the Galactic rotation (Brand & Blitz 1993) toward the tangential point ($l = 49^\circ$) of the Sagittarius spiral arm is ~ 60 km s⁻¹, the 68 km s⁻¹ cloud is associated with a high-velocity (HV) stream (Burton 1970). Carpenter & Sanders (1998) speculated that the massive star formation in W51 results from a collision between the W51 GMC and the 68 km s⁻¹ cloud which is related to a spiral density wave. Koo (1999) and Kumar et al. (2004) also argued that enhanced star formation in W51 might be caused by the spiral density wave.

In this paper we present new observations of W51 in the $J = 2 - 1$ transition of ^{12}CO and ^{13}CO lines. Our on-the-fly (OTF) maps are fully sampled in two lines simultaneously with an angular resolution of $32''$, and with rms noise per velocity channel of ~ 0.1 K in antenna temperature. Our sensitive, fully sampled mapping allows us to estimate mass more accurately and to delineate more detailed structure of the molecular gas. The purpose of this study is to find the correlation between the YSOs identified from the Galactic Legacy Infrared Mid-Plane Survey Extraordinaire (GLIMPSE I) Catalogs and the associated molecular clouds. We can approach the star formation history in this massive star-forming complex by analyzing CO data. In Section 2 we describe the observations and data processing. In Section 3 we present our analysis of the spectral features and describe indi-

¹ International Center for Astrophysics, Korea Astronomy and Space Science Institute, 838 Daedeokdaero, Yuseong, Daejeon 305-348, South Korea; mjokang@kasi.re.kr

² Department of Astronomy and Space Science, Chungnam National University, Daejeon 305-764, South Korea

³ Steward Observatory, University of Arizona, 933 North Cherry Avenue, Tucson, AZ 85721

vidual regions based on the CO, radio continuum, and *Spitzer* data. In Section 4 we discuss the spatial distribution of the H II regions and estimate the star formation efficiency. In Section 5 we summarize our main conclusions.

2. OBSERVATIONS AND PROCESSING

2.1. ^{12}CO and ^{13}CO $J = 2 - 1$ and ^{13}CO $J = 1 - 0$

The W51 GMC complex was mapped in the $J = 2 - 1$ transition of ^{12}CO and ^{13}CO with the 10 meter Heinrich Hertz Telescope (HHT) on Mount Graham, Arizona. The first observation was in 2005 November. A $1^\circ 25' \times 1^\circ 00'$ mapping centered on $(l, b) = (49^\circ 375, -0^\circ 200)$ was completed in 2008 February. The whole map consists of a total of 15 sub-fields. Each of the $15' \times 20'$ sub-fields was mapped with OTF scanning in right ascension at $10''$ per second with a row spacing of $10''$ in declination. Prior to 2006 December, we used a single-polarization double sideband SIS mixer receiver with system temperatures of typically 350 – 500 K, depending on weather and source elevation. Since 2006 December, the observations were made using the 1.3 mm ALMA dual-polarization sideband-separating receiver with a 4-6 GHz intermediate frequency band. The receiver was tuned to the ^{12}CO $J = 2 - 1$ line at 230.538 GHz in the upper sideband and the ^{13}CO $J = 2 - 1$ line at 220.399 GHz in the lower sideband. Typical system temperatures were in the range 180 – 300 K. The spectrometers, one for each of the two polarizations and the two sidebands, were filter banks with 256 channels of 1 MHz width and separation (corresponding to a velocity resolution of 1.3 km s $^{-1}$ for the ^{12}CO $J = 2 - 1$ line). For some subfields of the ^{12}CO $J = 2 - 1$ mapping, the spectra were measured with an acousto-optic spectrometer (AOS) having a frequency resolution of 1 MHz, and a total bandwidth of 1 GHz. The main beam efficiency, measured from planets, was 0.85 with an estimated uncertainty of (+0.05, -0.10).

The raw data were processed with the CLASS reduction package (from the University of Grenoble Astrophysics Group). The intensity scales for the two polarizations were determined from observations of W51D made just before the OTF maps. System temperatures were checked by the standard ambient temperature load method (Kutner & Ulich 1981) after every other row of the map grid. Further analysis was done with the MIRIAD software package (Sault et al. 1995). Although the data observed early in the program with a different receiver were noisier than the data obtained using the ALMA receiver, data quality was improved after combining all of the data using a $(1/T_{\text{sys}})^2$ weighting. At the final step, the data were convolved with a $16''$ (FWHM) Gaussian beam, giving a $36''$ effective resolution from the original angular resolution of the telescope, $32''$ (FWHM). The two polarizations were averaged for each sideband, yielding images with rms noise per velocity channel of 0.16 and 0.07 K in T_A^* for the ^{12}CO $J = 2 - 1$ and ^{13}CO $J = 2 - 1$ respectively. The average rms noise level of the ^{12}CO map is larger than ^{13}CO because several sub-fields of ^{12}CO map were observed just once with the noisier receiver. The full set of HHT data will be made available in a separate paper (Bieging et al. 2010, in preparation).

We obtained ^{13}CO $J = 1 - 0$ data for the same region

from the Galactic Ring Survey (GRS)⁴ (Jackson et al. 2006). Their spectral resolution is 0.2 km s $^{-1}$, and the angular resolution and sampling are $46''$ and $22''$, respectively. We transform antenna temperature of ^{13}CO $J = 1 - 0$ of GRS to main beam temperature, dividing by a main beam efficiency of 0.48.

2.2. *Spitzer* Data

The Galactic Legacy Infrared Mid-Plane Survey Extraordinaire (GLIMPSE I; Benjamin et al. 2003) covered the Galactic plane ($10^\circ < |l| < 65^\circ$, $|b| < 1^\circ$) with the four mid-IR bands of the Infrared Array Camera (IRAC; Fazio et al. 2004) on the *Spitzer* Space Telescope. Each IRAC band contains different spectral features: Band 1 ($3.6 \mu\text{m}$) shows mainly continuum emission from stars, Band 2 ($4.5 \mu\text{m}$) traces H $_2$ rotational transitions arising in the shocked gas associated with outflows, and emission in Bands 3 ($5.8 \mu\text{m}$) and 4 ($8.0 \mu\text{m}$) is dominated by polycyclic aromatic hydrocarbon (PAH) features. For this study, we have retrieved images of the $1^\circ 25' \times 1^\circ 00'$ region of W51 centered on $(l, b) = (49^\circ 375, -0^\circ 200)$ by combining two mosaic images which have a high resolution of $1''.2$. For the same region, we used the GLIMPSE I Catalog to extract point sources that are detected at least twice in one band with an S/N > 5. The GLIMPSE I Catalog also tabulates JHK_s flux densities from the Two Micron All Sky Survey (2MASS) point source catalog (Skrutskie et al. 2006) for all GLIMPSE sources with 2MASS identifications.

MIPSGAL (Carey et al. 2005) is a legacy program covering the inner Galactic plane, $10^\circ < |l| < 65^\circ$ for $|b| < 1^\circ$, at 24 and $70 \mu\text{m}$ with the Multiband Imaging Photometer for *Spitzer* (MIPS; Rieke et al. 2004) Space Telescope. The resolution of the $24 \mu\text{m}$ mosaics from the MIPSGAL survey is $2''.4$. We extracted $24 \mu\text{m}$ point-sources with $F/\delta F > 7$, then bandmerged the $24 \mu\text{m}$ sources with the GLIMPSE Catalog sources using a $2''.0$ correlation radius. The final source list contains data from all 8 bands: 2MASS (JHK_s), GLIMPSE (IRAC 1, 2, 3, 4 bands), and MIPSGAL $24 \mu\text{m}$. A total of 104,582 sources within the target region were selected from the GLIMPSE I Catalog. In an earlier paper, Kang et al. (2009b) examined this set of point sources to identify and classify YSOs near the W51 H II region complex using spectral energy distribution (SED) fits. All 8 bands are used for SED fitting as long as detected.

3. RESULTS

3.1. Velocity Structure

Toward the W51 H II region complex, most ^{12}CO emission comes from velocity intervals of $V_{\text{LSR}} = 0\text{--}25$ km s $^{-1}$ and $35\text{--}75$ km s $^{-1}$ (Carpenter & Sanders 1998). We do not consider the former velocity component, which originates from nearby molecular clouds. We focus on the later velocity component, which is extended from 30 to 85 km s $^{-1}$ in our sensitive and small grid mapping, associated with the W51 H II region complex.

Figure 1 represents the ^{12}CO $J = 2 - 1$ intensity map integrated over the velocity range between 30 and 85 km s $^{-1}$. Most of the bright ^{12}CO $J = 2 - 1$ emission peaks are coincident with bright radio continuum sources. The

⁴ <http://www.bu.edu/galacticring/>

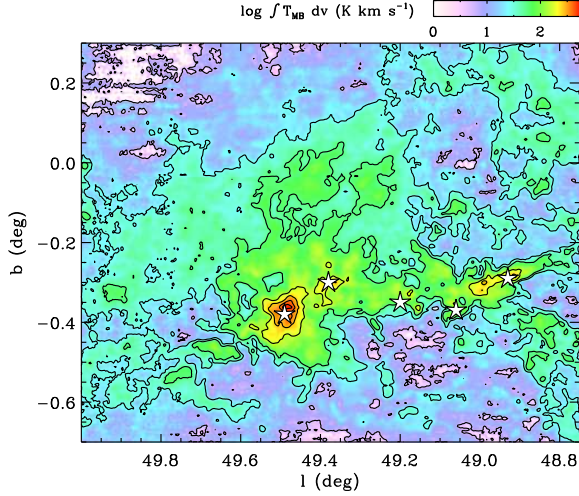


FIG. 1.— Distribution of the $^{12}\text{CO } J=2-1$ emission in the W51 H II region complex. The $^{12}\text{CO } J=2-1$ emission is integrated from 30 to 85 km s^{-1} . The contour levels are 1, 5, 10, 30, 50, 70, and 90% of the peak value (542 K km s^{-1}) in the map. Star symbols mark the thermal radio continuum sources listed by Goss & Shaver (1970). The names of the H II regions are G49.5-0.4, G49.4-0.3, G49.2-0.3, G49.1-0.4, and G48.9-0.3, from east to west.

W51 H II region complex shows a complicated structure in wide velocity ranges. Carpenter & Sanders (1998) divided molecular clouds associated with W51 into seven components at 44, 49, 53, 58, 60, 63, and 68 km s^{-1} . In W51A, the 53 km s^{-1} component is associated with G49.4-0.3 and the 58, 60, 63 km s^{-1} components are associated G49.5-0.4. The 68 km s^{-1} cloud is related to W51B. Besides the bright emission associated with radio continuum sources, there is $^{12}\text{CO } J=2-1$ emission extended over the whole of the $1^\circ 25' \times 1^\circ 00'$ region. More detailed structures of ^{12}CO and $^{13}\text{CO } J=2-1$ emission are shown in channel maps (Figures 2 and 3).

In the 43 and 46 km s^{-1} channel maps of Figure 2, there are molecular clouds not associated with the radio continuum sources. Some clouds are parallel to the Galactic plane at $b = 0^\circ$, and the others in the western⁵ part of the map are above the Galactic plane. CO emission in the W51A region appears in the first channel, 43 km s^{-1} . Especially at the position of the brightest radio continuum source, G49.5-0.4, the CO emission is distributed through the whole velocity range from 46 to 76 km s^{-1} . In contrast, the continuum sources of W51B are coincident with the filamentary structure with velocity $\geq 64 \text{ km s}^{-1}$, which we discuss below. As pointed out by Carpenter & Sanders (1998), the W51 molecular clouds with velocities of 58, 63 km s^{-1} are extended through a large area of the map, and the southern edge of the diffuse emission seen in the 64 km s^{-1} channel map is seen against the filamentary structure of 67 km s^{-1} . Two holes appear in the northern ($l, b = 49^\circ 50', -0^\circ 30'$) and eastern ($l, b = 49^\circ 60', -0^\circ 35'$) parts of G49.5-0.4 from 49 to 64 km s^{-1} (Figure 2).

Figure 4 shows the total CO distribution around W51 in three velocity ranges, 30 – 55, 56 – 65, and 66 – 85

⁵ Note: In this paper, directions are with reference to galactic coordinates, i.e., “north” means toward increasing latitude and “east” means toward increasing longitude.

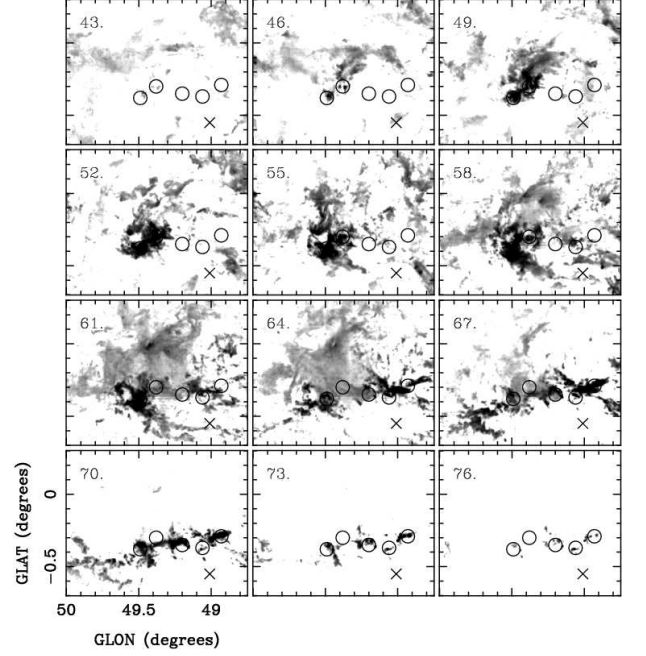


FIG. 2.— Channel maps of the $^{12}\text{CO } J=2-1$ emission averaged in 3 km s^{-1} intervals over the velocity range from 43 to 76 km s^{-1} . The values printed in the top left corner of each panel denote the center of the velocity intervals. The gray scale in each panel is a logarithmic stretch from log 1.0 K (white) to log 10.0 K in T_{MB} (black). Open circle symbols mark the thermal radio sources, and cross symbol represents the non-thermal radio source listed by Goss & Shaver (1970).

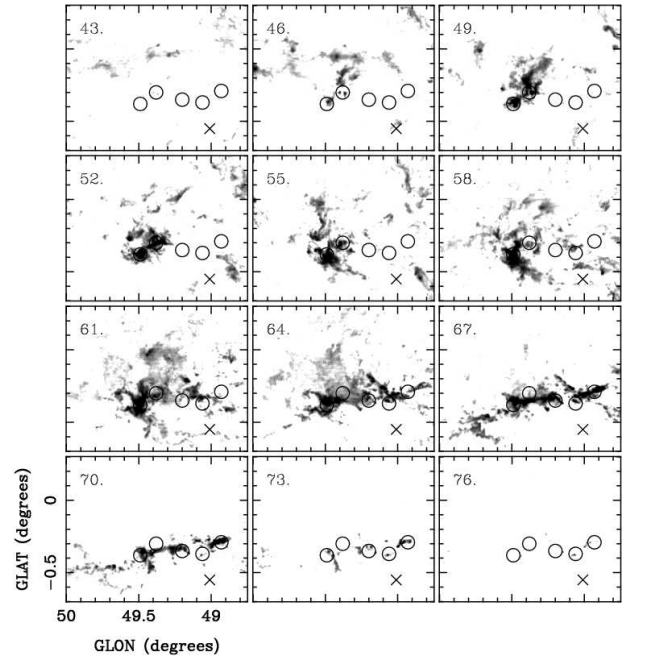


FIG. 3.— Same as Fig. 2, for $^{13}\text{CO } J=2-1$. The gray scale in each panel is a logarithmic stretch from log 0.3 K (white) to log 4.0 K in T_{MB} (black).

km s^{-1} . The molecular clouds associated with each radio continuum source show a range of different velocity structure. The white boxes outline the regions that we have analyzed to estimate the physical quantities from the ^{12}CO and $^{13}\text{CO } J=2-1$ data.

TABLE 1
 PHYSICAL PARAMETERS^a

Name ^b	Selected area				Velocity range ^c	Mass ^d	A_V ^e	$^{13}R_{2-1/1-0}$ ^f	$^{13/12}R_{2-1}$ ^g
	$l_{\min} (^{\circ})$	$l_{\max} (^{\circ})$	$b_{\min} (^{\circ})$	$b_{\max} (^{\circ})$	(km s^{-1})	($10^4 M_{\odot}$)	(mag)		
G49.5-0.4	49.42	49.60	-0.45	-0.29	49 – 72	8.7	72	0.87	0.31
G49.4-0.3	49.32	49.44	-0.36	-0.23	47 – 55	3.7	26	1.01	0.26
G49.2-0.3	49.13	49.29	-0.42	-0.27	62 – 73	3.8	21	0.78	0.25
G49.1-0.4	49.04	49.13	-0.42	-0.31	56 – 76	1.6	20	0.98	0.23
G49.17-0.21	49.13	49.21	-0.24	-0.18	58 – 69	0.9	20	0.78	0.37
G49.10-0.27	49.06	49.14	-0.31	-0.24	58 – 70	1.3	22	0.83	0.25
G49.0-0.3	48.96	49.03	-0.34	-0.26	62 – 75	1.5	26	1.14	0.21
G48.9-0.3	48.85	48.96	-0.32	-0.24	63 – 74	1.9	26	1.16	0.20
Shell	49.60	49.77	-0.24	-0.06	55 – 68	2.9	15	0.43	0.12
Cluster	49.30	49.55	-0.13	0.12	59 – 69	6.0	15	0.41	0.13
IRDC1	48.75	48.88	0.06	0.17	47 – 56	1.7	14	0.54	0.17
IRDC2	48.80	48.93	0.18	0.28	42 – 49	1.1	9	0.52	0.17

^a We assumed a distance of 6 kpc from the Sun to derive the physical parameters.

^b See Figure 4

^c Velocity range considered in the estimation of mass and line ratios

^d Mass derived using an LVG escape probability radiative transfer model

^e Peak A_V derived from the CO column density

^f Mean $^{13}\text{CO } J = 2 - 1 / J = 1 - 0$ intensity ratio

^g Mean $^{13}\text{CO} / ^{12}\text{CO } J = 2 - 1$ intensity ratio

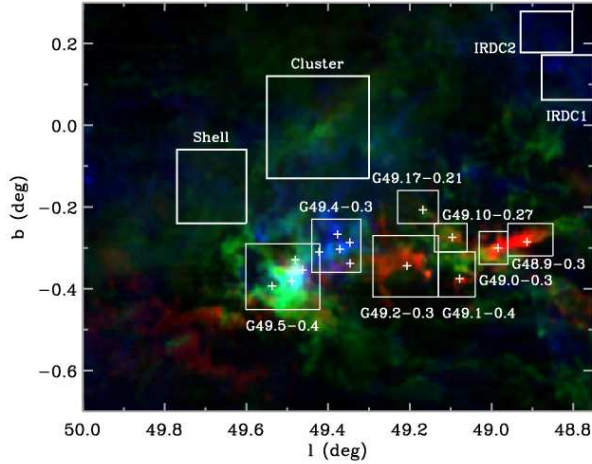


FIG. 4.— Color image of the W51 region composed of $^{12}\text{CO } J = 2 - 1$ intensity integrated over the velocity range of $30 - 55 \text{ km s}^{-1}$ (blue), $56 - 65 \text{ km s}^{-1}$ (green), and $66 - 85 \text{ km s}^{-1}$ (red). Cross symbols represent the compact radio continuum sources listed by Koo (1997). White boxes are the area for estimating the physical parameters in Table 1.

3.2. Line Ratios

Figure 5 shows the average spectra and ratios for all the regions marked with white boxes in Figure 4. CO line ratios are useful indicators of trends in line opacity and gas column density (isotopologue ratios, e.g., $^{13}\text{CO} / ^{12}\text{CO } J = 2 - 1$ ($\equiv ^{13/12}R_{2-1}$)); or of molecular excitation (e.g., $^{13}\text{CO } J = 2 - 1 / J = 1 - 0$ ($\equiv ^{13}R_{2-1/1-0}$)). As seen in Figure 5, G49.5-0.4 has a wide velocity range, from 45 to 75 km s^{-1} showing a peak at 60 km s^{-1} . The average $^{13}R_{2-1/1-0}$ value is 0.87 within the two vertical dotted lines. The selected velocity ranges, covering the strongest ^{13}CO emission, are associated with the H II regions or YSOs. The $^{13/12}R_{2-1}$ value increases with velocity up to around 65 km s^{-1} and then decreases. The spectrum of G49.4-0.3 shows a peak at a lower velocity, 51 km s^{-1} . The spectrum in W51B has strong emis-

sion between 55 and 75 km s^{-1} , which is different from the molecular cloud associated with the W51A region. The $^{13}R_{2-1/1-0}$ values of G49.2-0.3, G49.1-0.4, G49.10-0.27, G49.0-0.3, and G48.9-0.3 in W51B systematically increase in the higher velocity ranges (Figure 5). The ratio plots in Figure 5 generally show an anti-correlation between $^{13/12}R_{2-1}$ and $^{13}R_{2-1/1-0}$. In Table 1 we list the average $^{13}R_{2-1/1-0}$ and $^{13/12}R_{2-1}$ values derived from each region.

The average $^{13}R_{2-1/1-0}$ ratios associated with all H II regions are greater than 0.7, which implies that these clouds are relatively warm and dense. In contrast, the ratios of $^{13}R_{2-1/1-0}$ for the molecular clouds outside the active star-forming region, where there are no known continuum sources, are smaller than 0.7 (see Shell, Cluster, IRDC1, and IRDC2 in Figure 5). Molecular clouds with low ratios were often observed in dark clouds and outer envelopes of giant molecular clouds (Sakamoto et al. 1997).

3.3. Physical Properties

We use a non-LTE statistical equilibrium treatment of the CO molecular excitation to study physical properties of the molecular cloud. We apply the escape probability radiative transfer and photodissociation model of Kulesa et al. (2005) to our ^{12}CO and $^{13}\text{CO } J = 2 - 1$ data. We calculate grids of CO level populations for wide ranges of volume densities ($10^2 - 10^7 \text{ cm}^{-3}$) and temperatures ($5 - 300 \text{ K}$) assuming detailed balance and steady state. From these model grids, the total CO column density at each observed pixel is computed from the peak temperature, line widths and integrated intensities of the observed CO lines. The velocity range for integrating CO lines was determined from the range covering the strongest $^{13}\text{CO } J = 2 - 1$ emission on the line of sight (Figure 5). Assuming that the CO heating is dominated by photon processes (e.g., the photoelectric heating of dust), a coarse estimate of the incident radiation field can be made for each point in the map. The photodissociation model is then applied to estimate a total hydrogen column density from the CO data. This

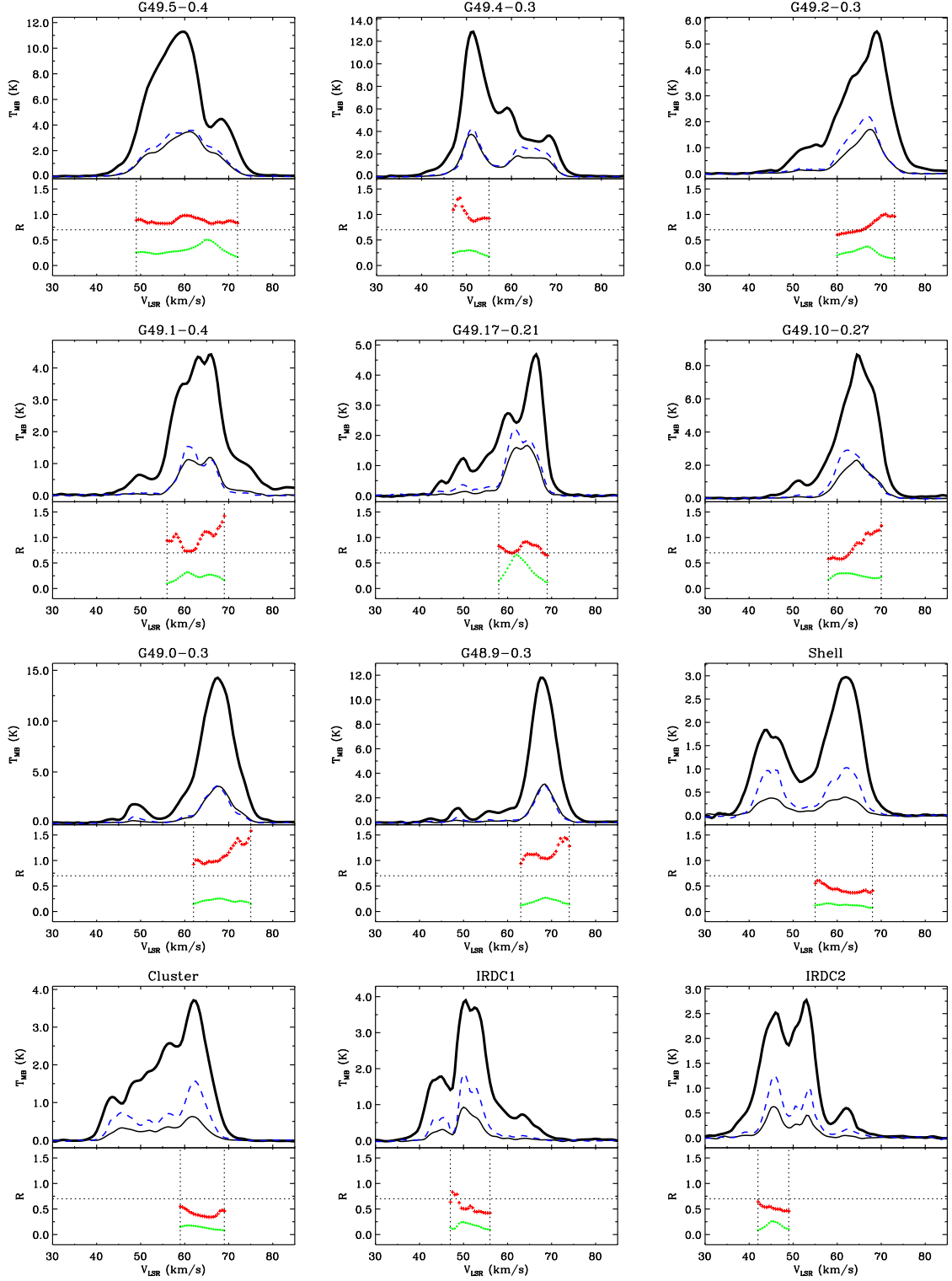


FIG. 5.— Average spectra of $^{12}\text{CO } J=2-1$ (thick line), $^{13}\text{CO } J=2-1$ (thin line), and $^{13}\text{CO } J=1-0$ (dashed line) and ratios of $^{13}R_{2-1/1-0}$ (red crosses) and $^{13/12}R_{2-1}$ (green dots) for the boxed areas in Figure 4. The horizontal dotted line is at 0.7 (see text). Two vertical dotted lines show the velocity range for deriving mass and the average line ratio of clouds, listed in Table 1. A typical uncertainty is smaller than marker.

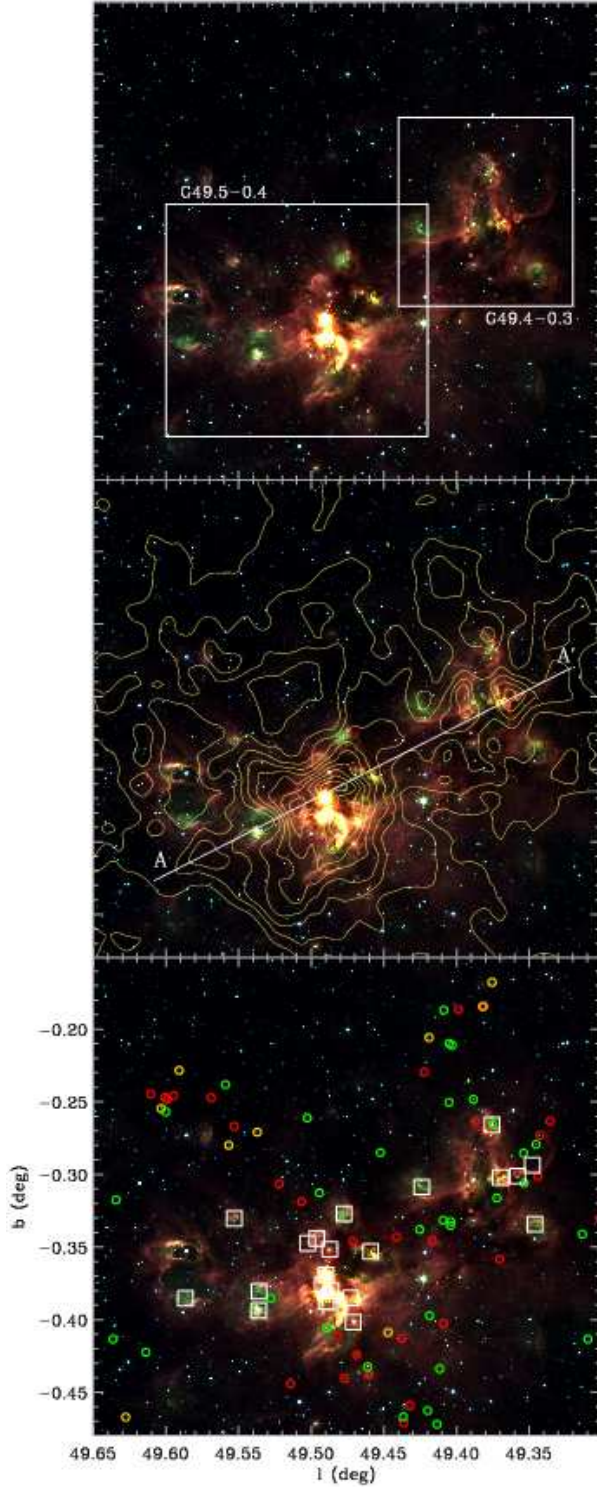


FIG. 6.— *Top*: Color image of the W51A region composed of IRAC 5.8 μm (red), 4.5 μm (green), and 3.6 μm (blue). White boxes show the area for analyzing the labeled radio continuum source in detail. *Middle*: Contour map of $^{12}\text{CO } J=2-1$ intensity integrated from 45 to 65 km s^{-1} . The contour levels are 40, 80, 120, 160, 200, 240, 280, 320, 360, and 400 K km s^{-1} . The oblique line shows the cut for the PV maps presented in Figure 7. *Bottom*: Squares are compact radio continuum sources listed by Mehringer (1994). YSO candidates (open circles) are marked in red for Stage 0/I, yellow for Stage II, and green for ambiguous sources.

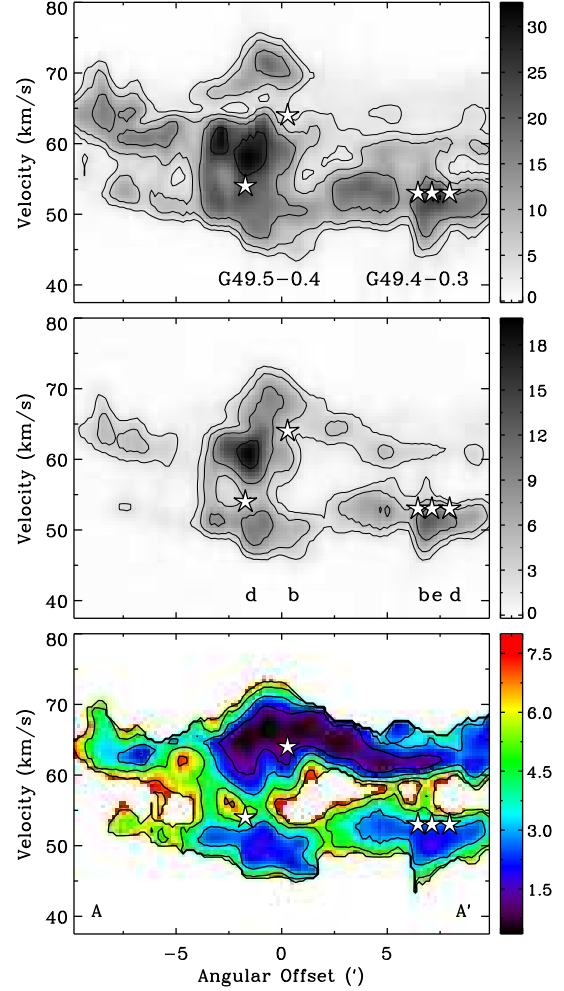


FIG. 7.— $^{12}\text{CO } J=2-1$ (top), $^{13}\text{CO } J=2-1$ (middle) and $^{12/13}\text{R}_{2-1}$ (bottom) position-velocity map through the W51 A region from southeast (A) to northwest (A') marked at the second panel of Figure 6. The temperature scale is indicated on the right (K in T_{MB}). Contour levels of $^{12}\text{CO } J=2-1$ and $^{13}\text{CO } J=2-1$ maps are 10, 20, 40, and 80% of peak value in the map. Contour levels of $^{12/13}\text{R}_{2-1}$ map are 1.5, 3.0, 5.0, and 7.0. Star symbols represent the position of the radio continuum sources (d and b of G49.5-0.4 and b, e, and d of G49.4-0.3). The velocities of the radio continuum sources come from the radio recombination line observations (van Gorkom et al. 1980; Pankonin et al. 1979).

calculation is based on the CO and H_2 photodissociation treatments of van Dishoeck & Black (1988) and Black & van Dishoeck (1987), respectively, using a total interstellar carbon abundance of $C/H = 2.4 \times 10^{-4}$ (Cardelli et al. 1996). Because the CO abundance is a strong function of column density, blind application of a uniform CO “dark cloud” abundance (10^{-4}) can lead to a gross underestimate of total hydrogen column density and gas mass. The visual extinction, A_V , is calculated from $N(\text{H})$ using $N(\text{H})/A_V = 1.9 \times 10^{21} \text{ cm}^{-2} \text{ mag}^{-1}$ (Bohlin et al. 1978). The distance to W51 derived in previous studies vary from 2.0 to 8.3 kpc. Figueredo et al. (2008) derived 2.0 ± 0.3 kpc by spectroscopic parallaxes of O-type stars. The kinematic distance is 5.5 kpc using radio recombination lines (Russeil 2003). The values de-

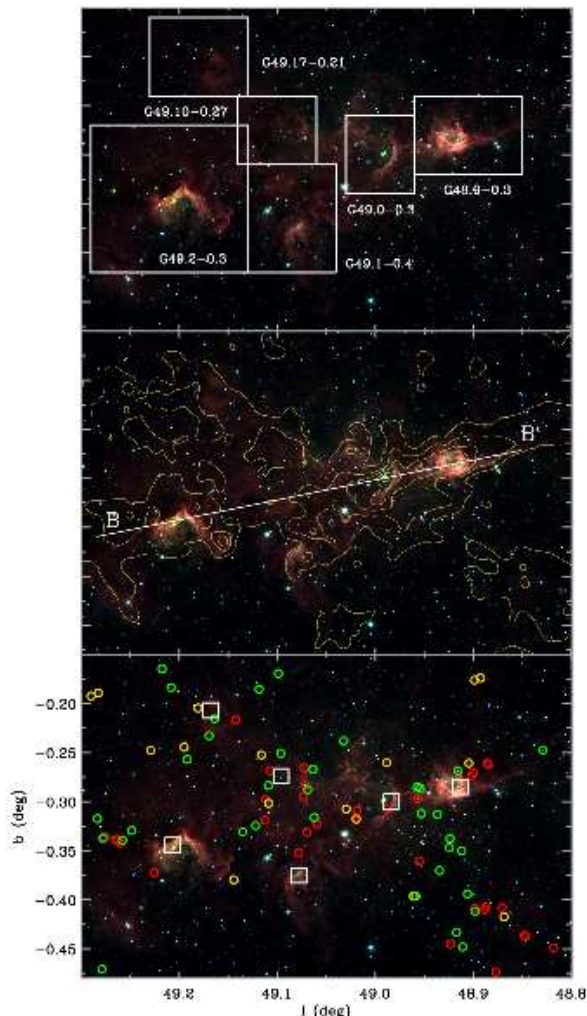


FIG. 8.— *Top*: Color image of the W51B region composed of IRAC 5.8 μm (red), 4.5 μm (green), and 3.6 μm (blue). White boxes show the area for analyzing the labeled radio continuum source in detail. *Middle*: Contour map of $^{12}\text{CO } J=2-1$ intensity integrated from 55 to 75 km s^{-1} . The contour levels are 30, 90, 150, 210, and 270 K km s^{-1} . The oblique line shows the cut for the position-velocity maps presented in Figure 9. *Bottom*: Squares are compact radio continuum sources listed by Koo (1997). YSO candidates (open circles) are marked in red for Stage 0/I, yellow for Stage II, and green for ambiguous sources.

rived from water maser proper motion measurements are 6.1 ± 1.3 kpc (Imai et al. 2002), 7 ± 1.5 kpc (Genzel et al. 1981), and 8.3 ± 2.5 kpc (Schneps et al. 1981). Recently, Xu et al. (2009) found the distance of $5.1^{+2.9}_{-1.4}$ kpc using trigonometric parallax measurements. In this paper, we adopt a distance of 6 kpc and use that value to calculate the gas masses of the selected regions shown in Figure 4. In Table 1, we list the size of the regions, velocity range, masses, extinctions, and the mean ratios of the lines.

3.4. Large Scale Structure

3.4.1. W51A

W51A includes the radio continuum sources G49.5-0.4 and G49.4-0.3 (Figure 6). G49.5-0.4 is the brightest component in radio continuum in the W51 re-

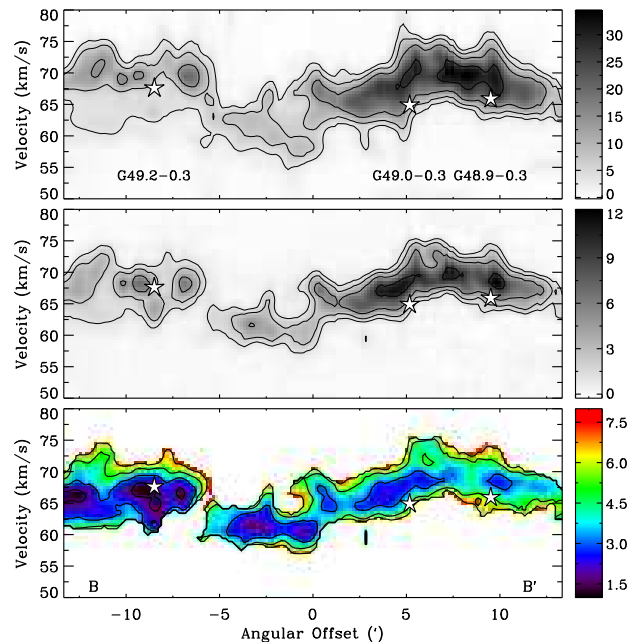


FIG. 9.— $^{12}\text{CO } J=2-1$ (top), $^{13}\text{CO } J=2-1$ (middle) and $^{12}/^{13} R_{2-1}$ (bottom) position-velocity map through the radio continuum sources G49.2-0.3, G49.0-0.3, and G48.9-0.3 from B to B' in Figure 8. The temperature scale is indicated on the right (K in T_{MB}). Contour levels of the $^{12}\text{CO } J=2-1$ and $^{13}\text{CO } J=2-1$ maps are 10, 20, 40, and 80% of the peak value in the map. Contour levels of the $^{12}/^{13} R_{2-1}$ map are 1.5, 3.0, 5.0, and 7.0. Star symbols represent the radio continuum sources. The RRL velocities of radio continuum sources are the mean velocities of the ionized gas (Pankonin et al. 1979).

gion. It contains the infrared sources W51 IRS1 and IRS2 (Wynn-Williams et al. 1974), and the H_2O masers W51 MAIN, W51N, and W51S (Genzel & Downes 1977). Mehringer (1994) found that G49.5-0.4 consists of 16 discrete components using the VLA radio continuum observations at 3.6, 6, and 20 cm. G49.4-0.3 located to the west of G49.5-0.4 is associated with 6 radio continuum sources (Mehringer 1994).

Figure 6 shows the distribution of mid-infrared and CO emission in W51A. The radio continuum sources detected by Mehringer (1994) are marked with squares and YSO candidates are marked with colored open circles. YSO candidates were identified and classified by Kang et al. (2009b) using the SED fitting tools of Robitaille et al. (2007). Each color represents the evolutionary stage of the YSO candidates: red for Stage I/0, yellow for Stage II, and green for ambiguous sources. Most YSO candidates in the W51A region are Stage I/0 (red) or ambiguous sources (green). The bright IRAC 4.5 μm emission (green) is seen at the position of the radio continuum sources. This 4.5 μm emission might be explained as line emission from H_2 in shocked molecular gas (Cyganowski et al. 2008; Davis et al. 2007; Shepherd et al. 2007; Smith et al. 2006).

Figure 7 shows $^{12}\text{CO } J=2-1$, $^{13}\text{CO } J=2-1$, and the ratio of $^{12}\text{CO } J=2-1$ to $^{13}\text{CO } J=2-1$ ($\equiv ^{12}/^{13} R_{2-1}$) in the form of position-velocity (PV) maps of G49.5-0.4 and G49.4-0.3 along the line shown in Figure 6 (middle). The PV maps illustrate the kinematic relationship of each radio continuum source and associated

molecular cloud in W51A. The radio continuum sources of G49.5-0.4 appear to be associated with the molecular cloud at 58 km s^{-1} , and the G49.4-0.3 sources with a 53 km s^{-1} molecular component. Figure 7 also shows the clumpiness of the HV stream as well as the spatial relationship between the radio continuum sources and the molecular clouds. The HV stream with velocity 68 km s^{-1} is strong in front of the G49.5-0.4 region, while the HV stream near G49.4-0.3 is weak.

3.4.2. W51B

W51B consists of six radio continuum sources: G49.2-0.3, G49.17-0.21, G49.10-0.27, G49.1-0.4, G49.0-0.3 and G48.9-0.3. In Figure 8, we mark the radio continuum sources listed by Koo (1997) on the three-color IRAC composite image. The molecular cloud toward the W51B region is distributed within the velocity range from 55 to 75 km s^{-1} . Figure 8 (middle) shows the $^{12}\text{CO } J = 2 - 1$ intensity integrated between 55 and 75 km s^{-1} , which is coincident with the bright IRAC emission. Most strong molecular clouds appear around the radio continuum sources. Eighty percent of the YSO candidates (lower panel) in W51B are early stage objects (Stage 0/I or ambiguous).

The H II regions of W51B are distributed parallel to the Galactic plane. Molecular clouds are distributed along $b \sim -0^\circ 3$. To analyze the detailed structure of each H II region and associated molecular cloud, we divide the W51B region into six groups: G49.2-0.3, G49.17-0.21, G49.10-0.27, G49.1-0.4, G49.0-0.3 and G48.9-0.3.

Figure 9 shows the PV maps of $^{12}\text{CO } J = 2 - 1$, $^{13}\text{CO } J = 2 - 1$ and $^{12/13}\text{R}_{2-1}$, through the three H II regions in the W51B region from B to B' in Figure 8 (middle). Most CO emission appears between 55 and 75 km s^{-1} . The molecular clouds associated with G48.9-0.3 and G49.0-0.3 are strong near 68 km s^{-1} . The $^{12/13}\text{R}_{2-1}$ ratio around G49.2-0.3 is smaller than 1.5 (red contours) at the offset position of $-7''.5$, which implies that the optical depth of the molecular gas is large at that position. Several YSOs are identified to the east of G49.2-0.3 ($l, b = 49^\circ 26', -0^\circ 34'$) on Figure 8. In Figure 9 (bottom), the molecular cloud associated with these YSOs, also shows a low ratio ($^{12/13}\text{R}_{2-1} < 1.5$), like the molecular cloud associated with G49.2-0.3.

3.5. Individual Regions

3.5.1. G49.5-0.4

Figure 10 shows the complicated structure of G49.5-0.4 in various wavelengths. Although the IRAC emission and the $^{13}\text{CO } J = 2 - 1$ integrated intensity show similar structure, the peak position of the $^{13}\text{CO } J = 2 - 1$ intensity coincides with a dark part of the IRAC composite image near the southeast region of component b. Some radio sources are located in the brightest part of the molecular cloud. Two bright radio continuum sources, W51d and W51e, coincide with the infrared sources IRS 2 and IRS 1 and are adjacent to two peaks of the integrated intensity map of the $^{13}\text{CO } J = 2 - 1$ emission. Other sources (a, b, f, g, h, and i) are located near the edge of the molecular cloud. These radio sources are coincident with the bright region in the IRAC $4.5 \mu\text{m}$ band (green) probably indicative of shocked H_2 .

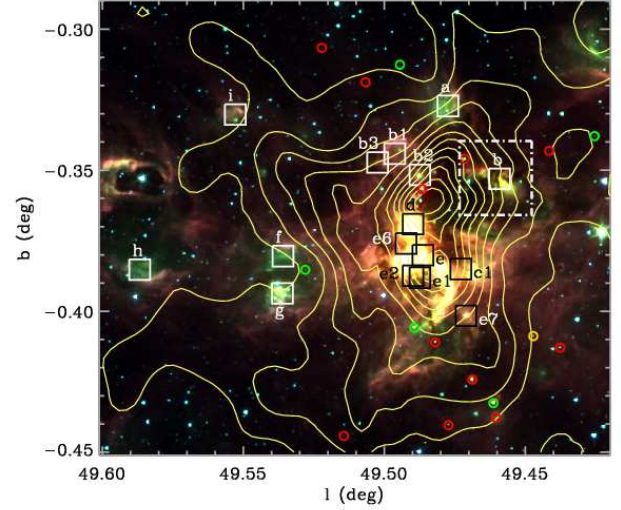


FIG. 10.— The $^{13}\text{CO } J = 2 - 1$ intensity integrated over the velocity range from 45 to 75 km s^{-1} overlaid on the color image of the G49.5-0.4 region composed of IRAC $5.8 \mu\text{m}$ (red), $4.5 \mu\text{m}$ (green), and $3.6 \mu\text{m}$ (blue). Contour levels are $20, 40, 60, 80, 100, 120, 140, 160, 180, 200, 220$, and 240 K km s^{-1} . Squares are the ZAMS OB stars listed by Mehringer (1994). YSO candidates (open circles) are marked in red for Stage 0/I, yellow for Stage II, and green for ambiguous sources. The dash-dotted rectangle shows the field in Figure 11.

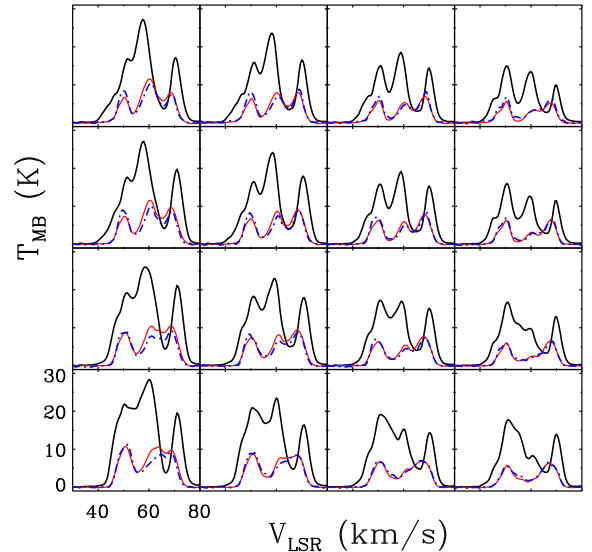


FIG. 11.— Tile map of the $^{12}\text{CO } J = 2 - 1$ (thick solid line), $^{13}\text{CO } J = 2 - 1$ (thin solid line), and $^{13}\text{CO } J = 1 - 0$ (dash-dotted line) spectra of G49.5-0.4 component b seen in the dash-dotted box in Figure 10. Spacing of the mapping grid is $22''$.

The spatial distribution of the radio continuum sources and associated molecular clouds can be constructed by comparing the velocity of ionized gas, CO emission, and absorption lines. The average velocity of the ionized gas is 59 km s^{-1} , which was measured using the $\text{H109}\alpha$ recombination line by Wilson et al. (1970). CO emission is brightest at $V_{\text{LSR}} = 61.0 \text{ km s}^{-1}$ (Figure 5). The ionized

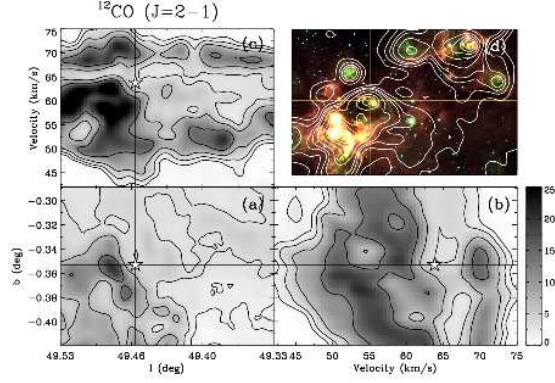


FIG. 12.— Spatial and position-velocity diagrams of component b of G49.5-0.4 in $^{12}\text{CO } J=2-1$. (a) is channel map at 64 km s^{-1} , which is RRL velocity. The star symbol represents component b of G49.5-0.4. (b) and (c) are position-velocity maps in latitude and longitude across the solid lines in (a). The ^{12}CO contour levels are 1.6, 3.2, 6.4, 12.8, and 25.6 K in T_{MB} . (d) is composite image of IRAC 5.8 μm (red), 4.5 μm (green), and 3.6 μm (blue). The contours show the 21 cm radio continuum emission (Koo & Moon 1997). The contour levels are 0.015, 0.05, 0.1, 0.15, 0.3, 0.6, 0.9, 1.2, 1.5, and 1.8 Jy beam^{-1} .

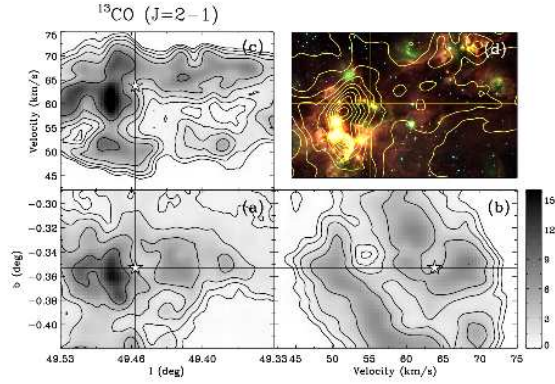


FIG. 13.— Same as in Figure 12, for $^{13}\text{CO } J=2-1$. The ^{13}CO contour levels are 0.5, 1.0, 2.0, 4.0, 8.0, and 16.0 K in T_{MB} . Contours on (d) show the $^{13}\text{CO } J=2-1$ intensity integrated from 42 to 75 km s^{-1} . The contour levels are 15, 45, 75, 105, 135, 165, 195, 225, 255, and 285 K km s^{-1} .

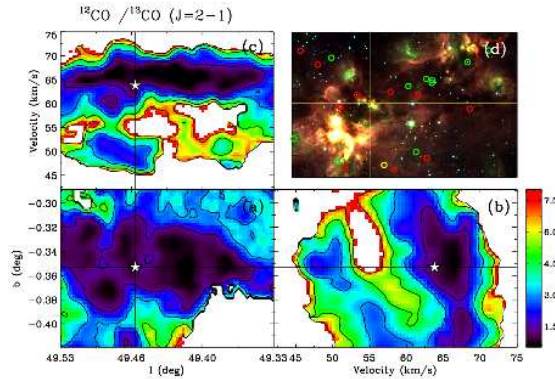


FIG. 14.— Same as in Figure 12, for ratio of $^{12}/^{13}R_{2-1}$. Contour levels are 1.5, 3.0, 5.0, and 7.0. YSO candidates (open circles) on (d) are marked in red for Stage 0/I, yellow for Stage II, and green for ambiguous sources.

and molecular gas have similar velocities, which implies that the molecular cloud at this velocity is associated with the radio continuum source. Toward G49.5-0.4, the central velocities of the ionized gas vary from 48 to 77 km s^{-1} (Mehringer 1994). H_2CO absorption has been detected between 52 and 73 km s^{-1} (Arnall & Goss 1985). H I 21 cm absorption has been observed at 50, 62, and 69 km s^{-1} (Koo 1997). H_2CO absorption between 66 and 70 km s^{-1} and H I absorption at 69 km s^{-1} implies that the HV stream is in front of G49.5-0.4. Regarding the spatial location of each radio continuum source in the G49.5-0.4 region, Arnall & Goss (1985) suggested that components a, b, and c are closer to the observer than components d and e by comparing the $\text{H}\alpha 109$ RRL and H_2CO absorption spectra. Koo (1997) reported that the H I cloud with 62 km s^{-1} velocity associated with G49.5-0.4, and components a, b, and e are either embedded in or behind this cloud while components f and g are located either in front of or the outside the cloud. Also, all radio continuum sources in the G49.5-0.4 region are spatially close because all H I spectra detected toward these sources have similar absorption profiles. Most of the bright radio components of G49.5-0.4 in the W51 H II region complex must be directly associated with the molecular clouds at 60 km s^{-1} .

CO spectra in the G49.5-0.4 region show complex structure. The average $^{12}\text{CO } J=2-1$ spectrum of G49.5-0.4 in Figure 5 is divided into two components with velocities of 59 and 68 km s^{-1} at the emission peaks. The brighter component between 45 to 65 km s^{-1} is associated with the radio continuum sources in G49.5-0.4. Figure 11 shows the CO spectra around component b of G49.5-0.4. There are three peaks in the $^{12}\text{CO } J=2-1$ emission at 52, 58, and 70 km s^{-1} . The intensities of $^{13}\text{CO } J=2-1$ and $J=1-0$ at 66 km s^{-1} are greater than $^{12}\text{CO } J=2-1$ intensities, which implies self-absorption in the $^{12}\text{CO } J=2-1$ emission. These CO self-absorption features clearly appear as a low ratio of $^{12}/^{13}R_{2-1}$ on PV maps inside the first contour (< 1.5) on Figure 7 (bottom).

Arnall & Goss (1985) proposed that component b of G49.5-0.4 is an H II regions created by O stars formed in the collision between the HV stream and the molecular cloud at 61-63 km s^{-1} . The RRL velocity of component b has been detected at 63.8 km s^{-1} in $\text{H}109\alpha$ (van Gorkom et al. 1980). Figures 12–14 show the spatial and kinematic structure around component b of G49.5-0.4 in ^{12}CO , $^{13}\text{CO } J=2-1$, and $^{12}/^{13}R_{2-1}$. As seen in Figures 12–14, component b lies between the main molecular cloud and the HV stream on the PV map. A clear difference between the PV maps of each CO isotopologue appears at 66 km s^{-1} . The $^{12}\text{CO } J=2-1$ intensity is very weak at the velocity between the main molecular cloud and the HV stream. However, the PV map of $^{13}\text{CO } J=2-1$ does not show an apparent boundary at this velocity so that $^{12}/^{13}R_{2-1}$ becomes small near 66 km s^{-1} . A deep absorption feature of H_2CO spectra (Fomalont & Weliachew 1973) and lower opacity molecular species such as $\text{CS } J=3-2$ (Penzias et al. 1971) and HCN (Snyder & Buhl 1971) have been detected at 66 km s^{-1} , which imply the presence of cold dense material in this region. In Figure 14(d) there are dark filamentary structures on the IRAC

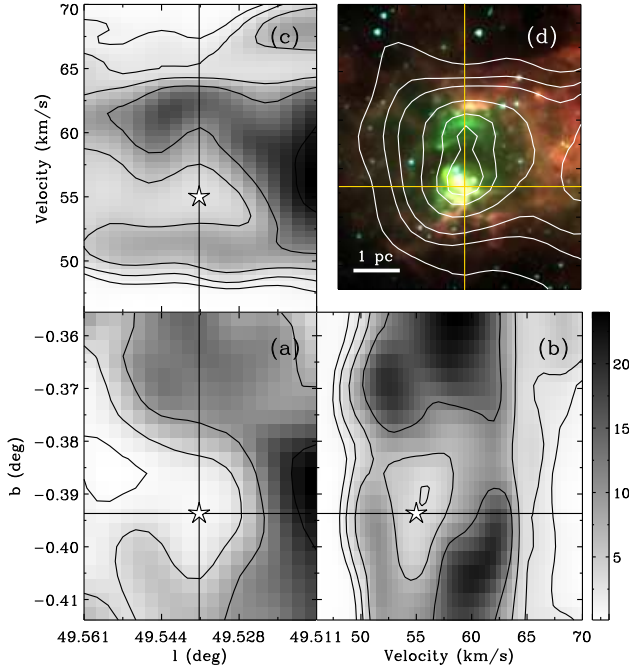


FIG. 15.— Spatial and position-velocity diagrams of component g of G49.5-0.4 in $^{12}\text{CO } J = 2 - 1$. (a) is the channel map at 55 km s^{-1} . The star symbol represents the component g. Contour levels are 1.5, 3, 6, and 12 K in T_{MB} . (b) and (c) are position-velocity maps in latitude and longitude across the solid lines in (a). (d) is the composite image of IRAC $5.8 \mu\text{m}$ (red), $4.5 \mu\text{m}$ (green), and $3.6 \mu\text{m}$ (blue). The contours show the 21 cm radio continuum emission (Koo & Moon 1997). The contour levels are 0.01, 0.03, 0.05, 0.10, 0.15, and $0.18 \text{ Jy beam}^{-1}$. Scale bar in the bottom left corner represents 1 pc at the distance of 6 kpc.

composite image. Several YSOs in very early stages are detected in the dark filaments which coincide with the inner area with $^{12/13}\text{R}_{2-1}$ of 1.5 (the first contour in Figure 14(a)).

Component g of G49.5-0.4 was observed at 54 km s^{-1} in [S III] emission line (Goudis & Hippelein 1982). The average $\text{H}\alpha$ velocity is $54.6 \pm 13.7 \text{ km s}^{-1}$ (Crampton et al. 1978). To investigate the velocity structure around component g, we present in Figure 15 the channel map at 55 km s^{-1} , which is the ionized gas velocity, and the position velocity map across component g. A prominent molecular gas cavity exists around component g in Figure 15(a). This cavity appears at a velocity of 55 km s^{-1} of both (b, v) (b) and (l, v) (c) maps. Figure 15(c) shows the velocity gradient from the expansion of molecular clouds around component g. In addition to the velocity structure, the green color in Figure 15(d) caused by the shocked H_2 emission is a strong evidence for the interaction of the ionizing star(s) and surrounding molecular cloud.

3.5.2. G49.4-0.3

G49.4-0.3 is located to the northwest of G49.5-0.4 and is composed of six subcomponents (Mehringer 1994). Figure 16 shows the detailed structure of G49.4-0.3 in $^{12}\text{CO } J = 2 - 1$ and IRAC bands. The bright emission

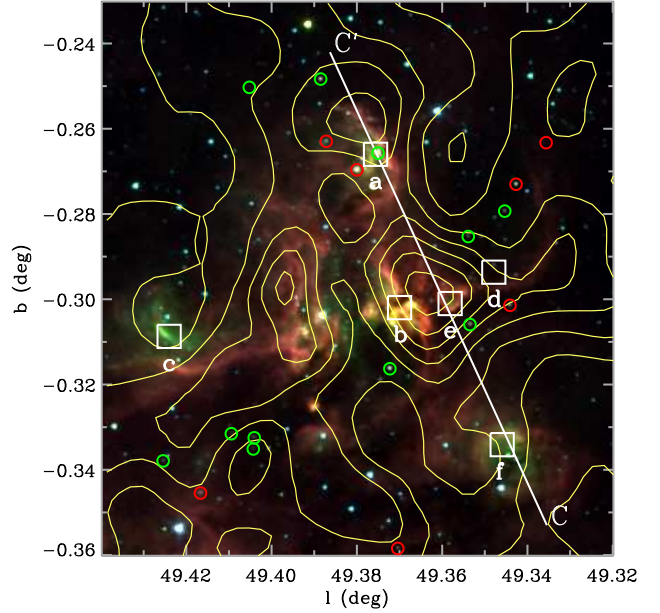


FIG. 16.— The $^{12}\text{CO } J = 2 - 1$ intensity integrated over the velocity range from 45 to 55 km s^{-1} overlaid on the color image of the G49.4-0.3 region composed of IRAC $5.8 \mu\text{m}$ (red), $4.5 \mu\text{m}$ (green), and $3.6 \mu\text{m}$ (blue). Contour levels are 25, 50, 75, 100, 125, 150, and 175 K km s^{-1} . Squares are the ZAMS OB stars listed by Mehringer (1994). YSO candidates (open circles) are marked in red for Stage 0/I, yellow for Stage II, and green for ambiguous sources. The oblique line shows the cut for the position-velocity map presented in Figure 17.

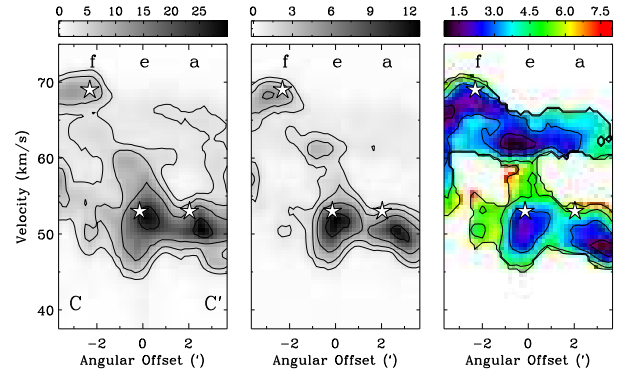


FIG. 17.— $^{12}\text{CO } J = 2 - 1$ (left), $^{13}\text{CO } J = 2 - 1$ (middle) and $^{12/13}\text{R}_{2-1}$ (right) position-velocity map through the radio continuum sources a, e, and f of G49.4-0.3 from northwest (C') to southeast (C) of the map in Figure 16. The temperature scale is indicated on the top (K in T_{MB}). Contour levels of the $^{12}\text{CO } J = 2 - 1$ and $^{13}\text{CO } J = 2 - 1$ maps are 10, 20, 40, and 80% of peak value in the map. Contour levels of the $^{12/13}\text{R}_{2-1}$ map are 1.5, 3.0, 5.0, and 7.0. Star symbols represent the position of the radio continuum sources. The velocity of a and e is the mean velocity of the ionized gas (Pankonin et al. 1979). The velocity of component f comes from the velocity of the molecular cloud around the radio continuum source.

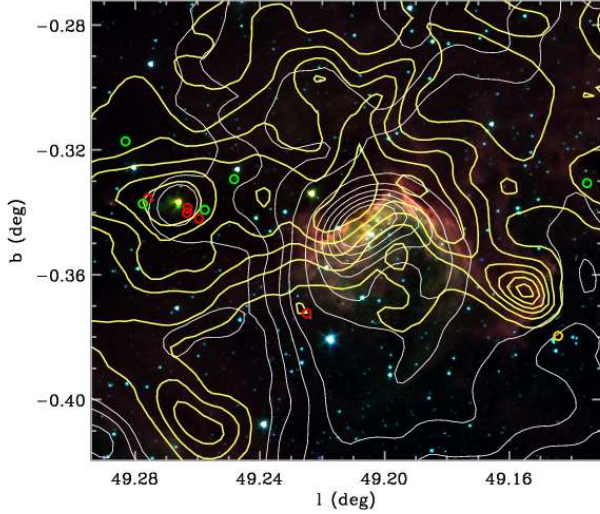


FIG. 18.— The $^{13}\text{CO } J=2-1$ intensity integrated over the velocity range from 57 to 76 km s^{-1} overlaid on the color image of the G49.2-0.3 region composed of IRAC 5.8 μm (red), 4.5 μm (green), and 3.6 μm (blue). Thick contour levels are 7, 14, 21, 28, 35, and 42 K km s^{-1} . Thin white contours show 21 cm radio continuum map. Contour levels are 0.015, 0.03, 0.06, 0.1, 0.3, 0.6, 0.9, 1.2, 1.5, and 1.8 Jy beam^{-1} (Koo & Moon 1997). YSO candidates (open circles) are marked in red for Stage 0/I, yellow for Stage II, and green for ambiguous sources.

in IRAC bands coincides with the $^{12}\text{CO } J=2-1$ intensity. Shocked bright 4.5 μm emission (green) appears around most radio continuum sources, except component d.

At least three different velocity components are shown in the average spectra of G49.4-0.3 (Figure 5). The brightest component at 52 km s^{-1} is associated with most of the radio continuum sources in G49.4-0.3 because the mean velocity of the ionized gas is at 53 km s^{-1} (Pankonin et al. 1979). However, the velocities of the individual components have not been measured. The H_2CO absorption for components b and c is observed at 51 and 63 km s^{-1} (Arnall & Goss 1985), and the H I absorption for components a, b, c, d, and f has velocities between 42 and 66 km s^{-1} (Koo 1997).

Figure 17 shows the PV map through components a, e, and f. In the $^{13}\text{CO } J=2-1$ PV map, there are three different velocity components. The brightest molecular cloud lies at 52 km s^{-1} , another at 62 km s^{-1} and the other at 69 km s^{-1} . All radio sources, except component f, are coincident with the molecular clouds at 52 km s^{-1} . The H I absorption at 53 km s^{-1} is dominant toward components a, b, c, and d, but for component f it is negligible (Koo 1997). Taking into account the dominant H I absorption and CO molecular cloud at the velocity of 69 km s^{-1} , component f is likely to be associated with the molecular cloud at 69 km s^{-1} .

3.5.3. G49.2-0.3

Figure 18 shows G49.2-0.3, which is the largest and brightest H II region in W51B, in IRAC bands as a three-color composite image, $^{12}\text{CO } J=2-1$ by thick yellow contours, and 21 cm radio continuum by thin

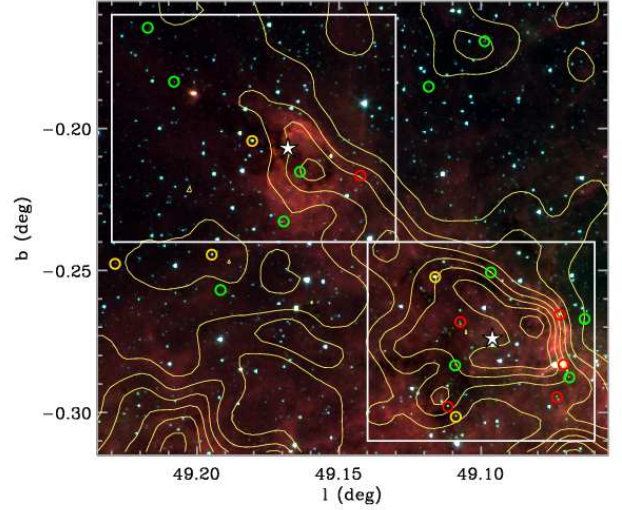


FIG. 19.— The $^{12}\text{CO } J=2-1$ intensity integrated over the velocity range from 55 to 75 km s^{-1} overlaid on the color image of the G49.17-0.21 and G49.10-0.27 region composed of IRAC 5.8 μm (red), 4.5 μm (green), and 3.6 μm (blue). Contour levels are 20, 40, 60, 80, 100, 120, and 140 K km s^{-1} . Star symbols are the radio continuum sources (Koo 1997). YSO candidates (open circles) are marked in red for Stage 0/I, yellow for Stage II, and green for ambiguous sources.

white contours. The radio continuum emission of G49.2-0.3 is apparently coincident with the bright region in IRAC bands. The 21 cm continuum brightness decreases rapidly toward the molecular cloud. The $^{12}\text{CO } J=2-1$ molecular cloud emission integrated between 57 and 76 km s^{-1} encompasses the half of the 21 cm radio continuum source toward the north. The morphology of the radio continuum source and the distribution of the CO emission indicate that G49.2-0.3 is a good example of blister type H II region (Israel 1978). The RRL velocity of the H II region is 67.6 km s^{-1} observed in H109 α by Pankonin et al. (1979) and the peak velocity of the $^{13}\text{CO } J=2-1$ emission averaged over all pixels shown in Figure 18 is 67.5 km s^{-1} (Figure 5). The H II region G49.2-0.3 forms on the boundary of the molecular cloud at 67.5 km s^{-1} . The $^{13}\text{CO } J=2-1$ emission is strong in the east side of the H II region where many YSOs appear around $(l, b = 49^\circ 26', -0^\circ 34')$. The peak velocity of $^{13}\text{CO } J=2-1$ emission is 68 km s^{-1} , which is close to the RRL velocity of G49.2-0.3. As discussed in the large scale structure of W51B, detailed velocity structure of CO lines through G49.2-0.3 and YSO clustering region is shown in Figure 9. These two regions divide into two different clumps on the $^{13}\text{CO } J=2-1$ PV map of Figure 9 (middle) and the integrated intensity map of Figure 18. The ratios of $^{12}/^{13}R_{2-1}$ are smaller than 1.5 at the position of H II region and the YSO clustering region around 66 km s^{-1} (Figure 9 bottom). The regions with the small ratios are associated with the star-forming activity.

3.5.4. G49.17-0.21 and G49.10-0.27

G49.17-0.21 and G49.10-0.27 are faint in IRAC bands, compared with other radio continuum sources in the

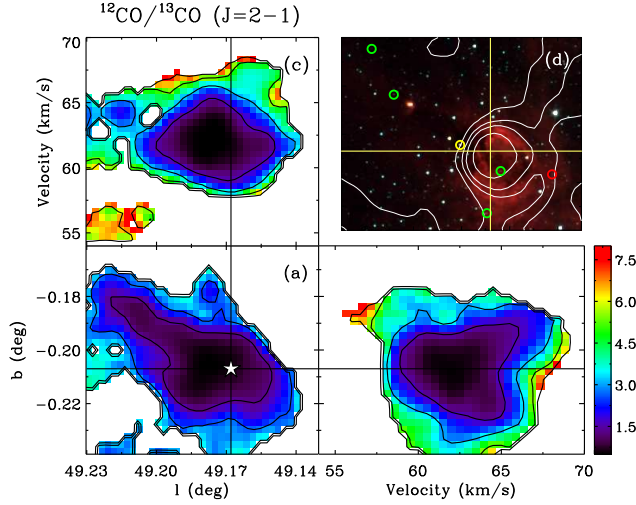


FIG. 20.— Spatial and position-velocity diagrams of G49.17-0.21 in $^{12}/^{13}R_{2-1}$. (a) is channel map at 61 km s⁻¹. (b) and (c) are position-velocity maps in latitude and longitude across the solid lines in (a). Contour levels are 1.5, 3.0, 5.0, and 7.0. (d) is composite image of IRAC 5.8 μm (red), 4.5 μm (green), and 3.6 μm (blue). The contours show the 21 cm radio continuum emission (Koo & Moon 1997). The contour levels are 0.01, 0.03, 0.05, and 0.10 Jy beam⁻¹. The star symbol is the radio continuum source (Koo 1997). YSO candidates (open circles) on (d) are marked in red for Stage 0/I, yellow for Stage II, and green for ambiguous sources.

W51B region (Figure 8). Figure 19 shows the ^{12}CO $J = 2 - 1$ intensity superposed on the IRAC three-color composite image. G49.17-0.21 is located in the northeast of the map. A cometary shape that consists of a head around the H II region and a tail toward northeast appears in all four IRAC bands as a dark feature. The ^{12}CO $J = 2 - 1$ integrated intensity map covers the bright IRAC emission around the H II regions over a large scale. The brightest CO emission coincides with the darker part of the IRAC image. In Figure 20, we present the ratio of $^{12}/^{13}R_{2-1}$ on the channel map of 61 km s⁻¹ and PV maps of G49.17-0.21. The region inside the first contour ($^{12}/^{13}R_{2-1} < 1.5$) coincides with the dark part of the IRAC image, where YSOs lie. The small ratio of $^{12}/^{13}R_{2-1}$ implies that the molecular cloud around G49.17-0.21 is exhibiting self-absorption in ^{12}CO $J = 2 - 1$. In the case of G49.10-0.27, a dark feature on the IRAC image appears around the H II region, where many YSOs are identified. The RRL velocity of 61 km s⁻¹ is measured only for G49.10-0.27 by Pankonin et al. (1979).

3.5.5. G49.1-0.4

Figure 21 shows the spatial and kinematic structure of the molecular cloud around G49.1-0.4. The molecular cloud consists of five clumps on the ^{12}CO $J = 2 - 1$ integrated intensity map (Figure 21(a)). Figure 22 shows the CO spectra at the peak positions of each clump in ^{13}CO $J = 2 - 1$. Clump 1 has a ^{13}CO $J = 2 - 1$ peak velocity of ~ 62 km s⁻¹. Clumps 2 and 3 have a ^{13}CO $J = 2 - 1$ peak velocity of ~ 66 km s⁻¹, which is similar to that of the H166 α RRL measured from G49.1-0.4 by Pankonin et al. (1979). CO emission of clumps 1, 2, and 3 is associated with the dark region on the IRAC compos-

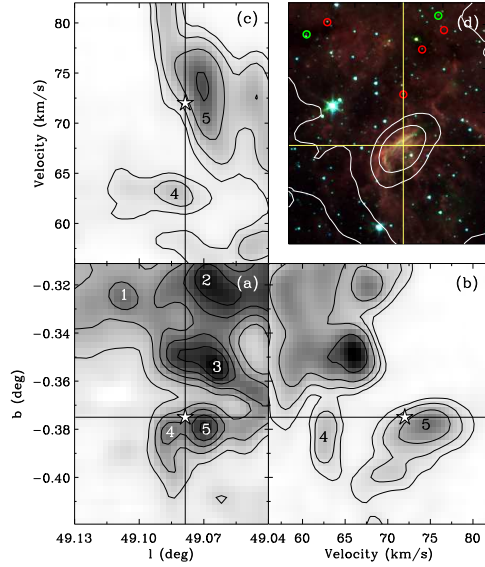


FIG. 21.— Spatial and position-velocity diagrams of G49.1-0.4 in ^{12}CO $J = 2 - 1$. (a) is the ^{12}CO $J = 2 - 1$ intensity integrated over the velocity range between 56 and 82 km s⁻¹. Contour levels are 30, 60, 90, 120, 150, and 180 K km s⁻¹. The grayscale is a stretch from 0 to 190 K km s⁻¹. Star symbol is the radio continuum source (Koo 1997). (b) and (c) are position-velocity maps in latitude and longitude across the solid lines in (a). Contour levels are 1.6, 3.2, 6.4, 13.0 K. The grayscale is a stretch from 0 to 20 K. (d) is the composite image of IRAC 5.8 μm (red), 4.5 μm (green), and 3.6 μm (blue). The contours show the 21 cm radio continuum emission (Koo & Moon 1997). The contour levels are 0.05, 0.10, 0.30, and 0.50 Jy beam⁻¹. YSO candidates (open circles) are marked in red for Stage 0/I, and green for ambiguous sources.

ite image and there are several YSOs in the early stage of evolution. Near the radio continuum source, there are two clumps: clump 4 refers to the 62 km s⁻¹ component and clump 5 refers to the 75 km s⁻¹ component.

It is significant that the ^{13}CO $J = 2 - 1$ intensity is stronger than the ^{13}CO $J = 1 - 0$ in clump 5 ($^{13}R_{2-1/1-0} > 2$). The high ratio of $^{13}R_{2-1/1-0}$ means that clump 5 is significantly different from the other clumps. Clump 5 seen in Figure 21(a) coincides with the bright IRAC composite emission and the 21 cm radio continuum emission seen in Figure 21(d). The RRL velocities in G49.1-0.4 are measured at 72.4 (H109 α), 70.9 (H109 α), 71.4 (H137 β) and 68 (H109 α) km s⁻¹ (Wilson et al. 1970; Pankonin et al. 1979; Downes et al. 1980). Assuming the velocity of ionized gas is 72 km s⁻¹, clump 5 is associated with G49.1-0.4 (Figure 21(b) and (c)). Comparing the ratios ($^{12}/^{13}R_{2-1}$ and $^{13}R_{2-1/1-0}$) at the ^{13}CO $J = 2 - 1$ peak of clumps 3 and 5, the excitation temperature of clump 5 is about three times higher than that of clump 3. The total mass of clump 5 is estimated to be $2.3 \times 10^3 M_{\odot}$ by a large velocity gradient (LVG) analysis using ^{12}CO and ^{13}CO $J = 2 - 1$ lines.

3.5.6. G49.0-0.3 and G48.9-0.3

G49.0-0.3 and G48.9-0.3 are located at the west edge of the W51B region (Figure 8). Figure 23 shows the ^{12}CO $J = 2 - 1$ emission superposed on the IRAC three color

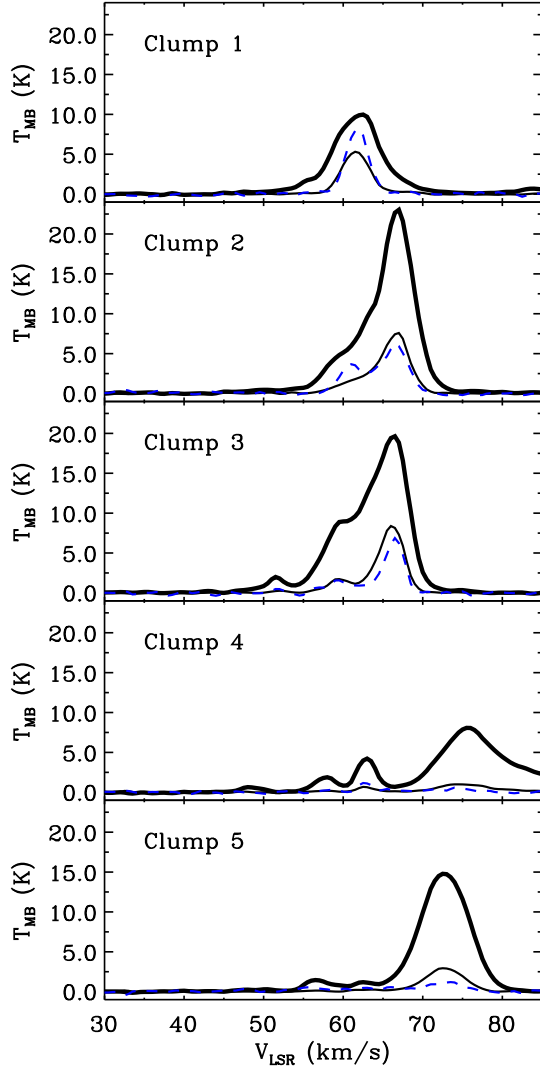


FIG. 22.— The $^{12}\text{CO } J = 2 - 1$ (thick solid line), $^{13}\text{CO } J = 2 - 1$ (thin solid line), and $^{13}\text{CO } J = 1 - 0$ (dash-dotted line) spectra at the peak position of each clump in Figure 21(a). The 75 km s^{-1} component in the fourth panel actually belongs to clump 5.

composite image. IRAC emission is very bright around the two radio continuum sources. The bright IRAC emission around G49.0-0.3 makes a bow shape, which has been observed as a faint K-band nebula (Kumar et al. 2004). Many stellar components seen as white spots are to the east of the bright bow. Kumar et al. (2004) found that G48.9-0.3 is composed of two sub-clusters in near-infrared J, H, K observations. These two sub-clusters also appear in the IRAC three-color composite image.

The average CO spectra of G49.0-0.3 and G48.9-0.3 in Figure 5 have a similar shape. Velocities of G49.0-0.3 and G48.9-0.3 at the $^{13}\text{CO } J = 2 - 1$ peak intensities are 67.5 and 68.5 km s^{-1} , respectively. The velocities of the ionized gas are measured at 64.9 and 64.4 km s^{-1} for G49.0-0.3 and G48.9-0.3 in the $\text{H}166\alpha$ line (Pankonin et al. 1979). The ratios of $^{13}R_{2-1/1-0}$ of G49.0-0.3 and G48.9-0.3 are large (> 0.7) around the RRL velocity, which indicates that the molecular clouds associated with the radio continuum sources are highly excited.

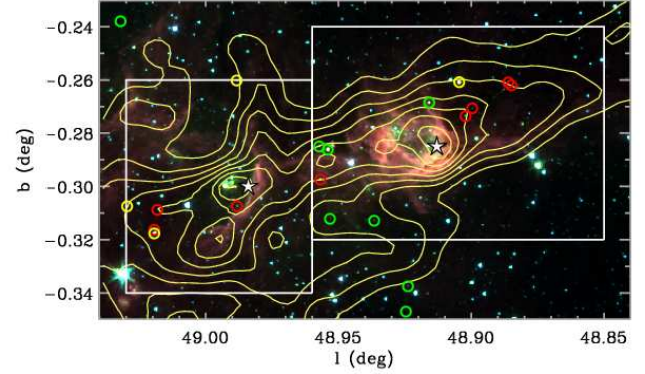


FIG. 23.— The $^{12}\text{CO } J = 2 - 1$ intensity integrated over the velocity range between 57 and 75 km s^{-1} overlaid on the color image composed of IRAC $5.8 \mu\text{m}$ (red), $4.5 \mu\text{m}$ (green), and $3.6 \mu\text{m}$ (blue) around the G49.0-0.3 and 48.9-0.3 region. Contour levels are $36, 72, 108, 144, 180, 216$, and 252 K km s^{-1} . Star symbols mark the radio continuum sources (Koo 1997). YSO candidates (open circles) are marked in red for Stage 0/I, yellow for Stage II, and green for ambiguous sources.

Many YSOs are found in the relatively dark region of the IRAC image along the filamentary structure of the molecular cloud. Two bright CO components are coincident with two radio continuum sources. We confirm that the dense regions are associated with the newly forming YSOs by comparing the distribution of YSOs and the $^{13}\text{CO } J = 2 - 1$ intensity on the channel maps. Figure 24 shows the $^{13}\text{CO } J = 2 - 1$ intensity in the velocity range from 61 to 75 km s^{-1} per 1 km s^{-1} . There are three groups of YSOs: one to the east of G49.0-0.3, another to the west of G48.9-0.3, and the other between G49.0-0.3 and G48.9-0.3. Dense molecular clouds associated with each group lie in different velocity ranges. YSOs between G49.0-0.3 and G48.9-0.3 are coincident with the high column density region from the 68 km s^{-1} channel. As seen in the PV diagram of $^{13}\text{CO } J = 2 - 1$ in Figure 9 (middle), there are three dense molecular clumps around G49.0-0.3 and G48.9-0.3. While the two clumps located on either side of the whole cloud are associated with radio continuum G49.0-0.3 and G48.9-0.3, the molecular clump between the two H II regions lies toward higher velocity. These two H II regions form an expanding arc of gas in PV diagram (Moon & Park 1998) (Figure 9).

4. DISCUSSION

4.1. Spatial Distribution of the Gas, YSOs, and Radio Continuum Sources

Comparing the velocities of our CO data to the velocities of RRL, H_2CO and HI absorption (Arnal & Goss 1985; Bieging 1975; Downes et al. 1980; Koo 1997; Mufson & Liszt 1979; Pankonin et al. 1979) discussed in previous sections, we deduce the spatial distribution of the W51 complex. The spatial distribution of the H II regions and YSOs around the central active star-forming region is shown in Figure 25. Many small clusters of 5-10 YSOs are apparent. Five of them are marked by large circles which happen to be close to PV cuts. Figures 26–28 show the velocity structure of $^{12}\text{CO } J = 2 - 1$, $^{13}\text{CO } J = 2 - 1$, and $^{12/13}R_{2-1}$ from $b = -0^\circ.45$ to $b = -0^\circ.20$ by a $0^\circ.05$ step. We compare the spatial distribution of the H II regions and the YSO clusters to the latitude-

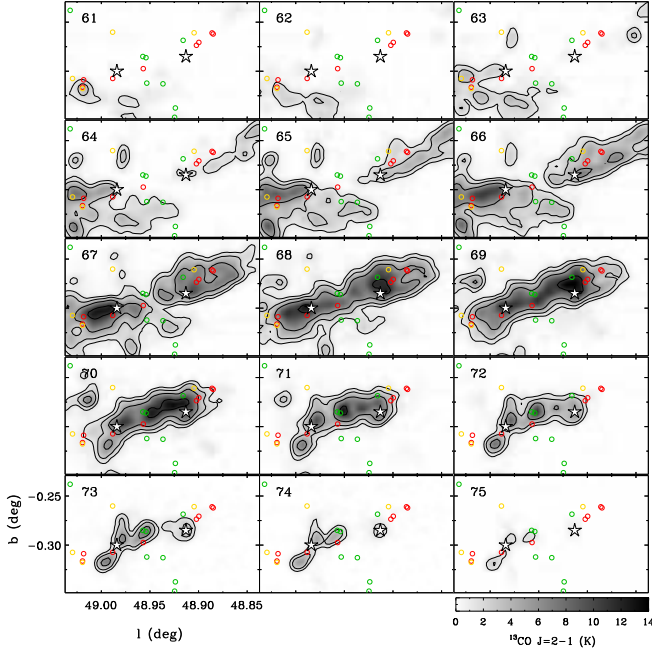


FIG. 24.— Channel maps of G48.9-0.3 and G49.0-0.3 in the $^{13}\text{CO } J=2-1$ emission over the velocity range from 61 to 75 km s^{-1} . Contour levels are 1.3, 2.6, 5.2, and 10.4 K in T_{MB} . Star symbols are the radio continuum sources (Koo 1997). YSO candidates (open circles) are marked in red for Stage 0/I, yellow for Stage II, and green for ambiguous sources.

velocity (l, v) maps of $^{12}\text{CO } J=2-1$, $^{13}\text{CO } J=2-1$, and their ratio ($^{12/13}R_{2-1}$) to determine the relative positions of the molecular clouds associated with the H II and YSO cluster regions. The brightest H II region, G49.5-0.4 extends from $b = -0^\circ45$ to $b = -0^\circ30$. The mean RRL velocity of 59 km s^{-1} agrees with the strong ^{12}CO and $^{13}\text{CO } J=2-1$ intensity. Most of the G49.4-0.3 sources are located on the $b = -0^\circ30$ line; their mean RRL velocity is 52 km s^{-1} . As seen on the section of $b = -0^\circ30$ in Figures 26–28, two strong components of molecular gas are located at 52 km s^{-1} and 68 km s^{-1} . Those are associated with G49.4-0.3 and G49.0-0.3. The HV molecular components over 70 km s^{-1} in W51A are not evident on the $b = -0^\circ30$ line. In Figures 26–28, the dense molecular cloud around $(l, v) = (49^\circ40, 50 \text{ km s}^{-1})$ in $b = -0^\circ25$ is associated with component of G49.4-0.3 and one around $(l, v) = (49^\circ20, 61 \text{ km s}^{-1})$ in $b = -0^\circ20$ is connected with G49.17-0.21. The radio continuum sources and the associated molecular cloud in W51A are behind the HV streaming gas considering H_2CO absorption line velocities. The HV streaming gas in front of G49.5-0.4 is much brighter in CO and more extended than that of G49.4-0.3. Spatially, G49.4-0.3 at 52 km s^{-1} is located behind G49.5-0.4 at 58 km s^{-1} . Most of the bright molecular clouds in W51B are within the velocity range of the HV stream. Toward G49.0-0.3 and G48.9-0.3, no other molecular clouds are observed in the lower velocity range. The sources of W51B within the HV streaming gas are located nearest to the Sun.

YSOs showing clustering are embedded in their parent molecular cloud. We find the positions of molecular clouds associated with YSOs by comparing Figure 25 with Figures 26–28. First, many YSOs are concentrated

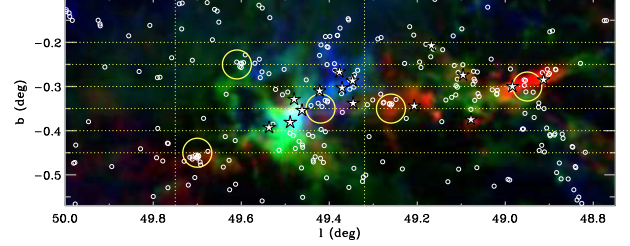


FIG. 25.— Spatial distribution of the H II regions (stars) and YSOs (small open circles) in the W51 complex, overplotted on a color image composed of $^{12}\text{CO } J=2-1$ intensity integrated over velocity range 30–55 km s^{-1} (blue), 56–65 km s^{-1} (green), and 66–85 km s^{-1} (red). The dotted horizontal lines are guide lines by 0.05° step. Two vertical dotted lines are guide lines for dividing W51A from W51B. Large thick open circles represent the YSO clustering regions.

around $(l, b) = (49^\circ68, -0^\circ45)$ in Figure 25. A molecular cloud is distributed around $(l, v) = (49^\circ68, 70 \text{ km s}^{-1})$ in the (l, v) map on $b = -0^\circ45$ (Figures 26–28). The second YSO cluster around $(l, b) = (49^\circ62, -0^\circ25)$ is associated with a molecular cloud around $(l, v) = (49^\circ62, 58 \text{ km s}^{-1})$ on $b = -0^\circ25$ in Figures 26–28. The third YSO cluster is located along the $b = -0^\circ35$ line between G49.5-0.4 and G49.4-0.3 (Figure 25). In Figure 28, the molecular cloud around $(l, v) = (49^\circ42, 65 \text{ km s}^{-1})$ at $b = -0^\circ35$ shows a small ratio of $^{12/13}R_{2-1}$ where the optically thick region coincides with the third YSO cluster. The fourth YSO cluster is near G49.2-0.3 at $(l, v) = (49^\circ28, 65 \text{ km s}^{-1})$ on $b = -0^\circ35$ in Figures 26–28. The fifth YSO cluster is located between G49.0-0.3 and G48.9-0.3 in Figure 25 and coincides with the molecular cloud at $(l, v) = (48^\circ95, 68 \text{ km s}^{-1})$ and $b = -0^\circ30$ in Figures 26–28. A schematic diagram showing the distribution of molecular clouds, the H II regions, and the YSO clusters is shown in Figure 29.

4.2. Triggered Star Formation

In this section, we discuss triggered star formation in W51. Triggered star formation was reviewed as three distinct mechanisms by Elmegreen (1998): (1) direct compression of clouds by supernovae, stellar winds, and H II regions (Klein et al. 1985), (2) collect and collapse (Elmegreen & Lada 1977), and (3) cloud collisions (Loren 1976).

The arc structure around G49.0-0.3 and G48.9-0.3 is likely to be an example of star formation triggered by the collect and collapse process. In a PV diagram through the two H II regions (Figure 9), the molecular cloud comprises a redshifted arc structure with $V_{\text{LSR}} = 60$ to 73 km s^{-1} (Moon & Park 1998). Two molecular clumps in this arc structure coexist with two H II regions. Another molecular clump is located at higher velocity than the locations of the two compact H II regions. Newly forming YSOs are associated with the dense molecular clumps (Figure 24). The shell structure near the W51A region (Figure 4) also shows evidence of star formation triggered by the expansion of an H II region, as discussed in an earlier paper (Kang et al. 2009a). Dense molecular material has been collected along the shell detected in *Spitzer* IRAC images. YSOs are identified toward the densest molecular condensation along the edge of the IRAC shell.

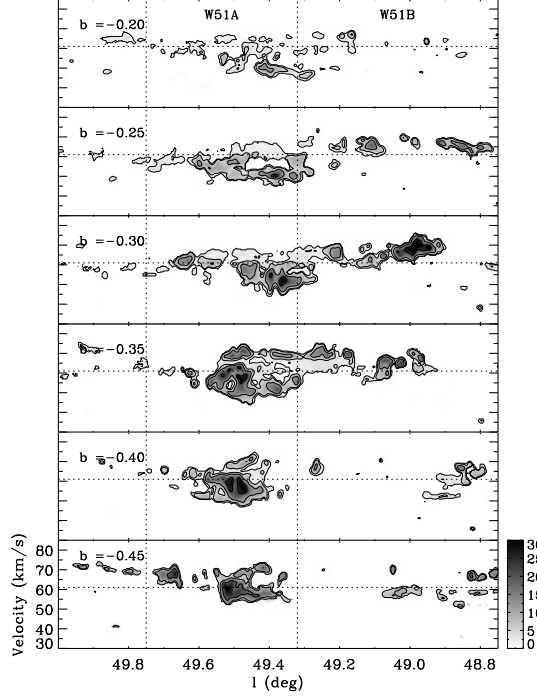


FIG. 26.— The longitude-velocity map of $^{12}\text{CO } J=2-1$ at fixed latitudes from $b = -0^\circ 20'$ to $b = -0^\circ 45'$ by $0^\circ 05'$ step. Contour levels are 3, 6, 12, and 24 K in T_{MB} . Two dotted vertical lines are guide lines for dividing the W51A and W51B regions. A dotted horizontal line shows the boundary of the HV streaming gas.

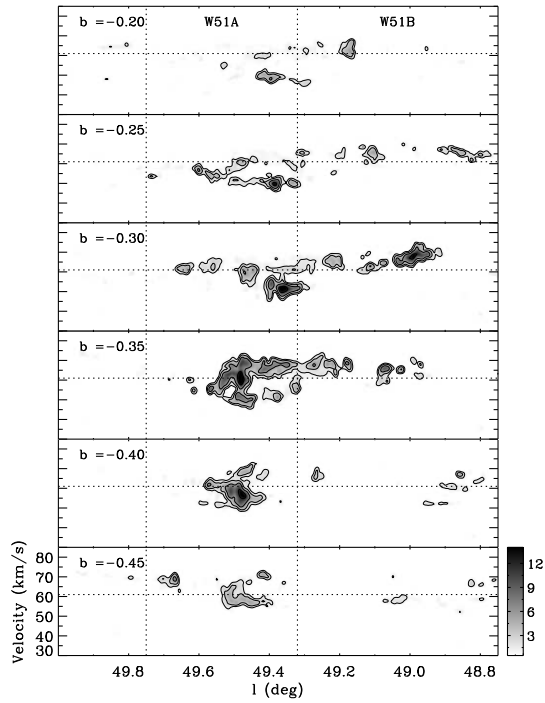


FIG. 27.— The longitude-velocity map of $^{13}\text{CO } J=2-1$ along the latitude from $b = -0^\circ 20'$ to $b = -0^\circ 45'$ by $0^\circ 05'$ step. Contour levels are 1.5, 3, 6, and 12 K in T_{MB} .

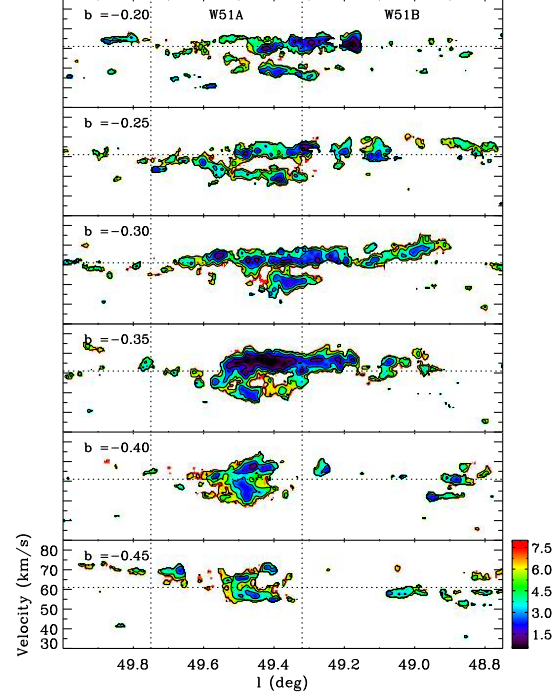


FIG. 28.— The longitude-velocity map of $^{12/13}\text{R}_{2-1}$ along the latitude from $b = -0^\circ 20'$ to $b = -0^\circ 45'$ by $0^\circ 05'$ step. Contour levels are 1.5, 3.0, 5.0, and 7.0.

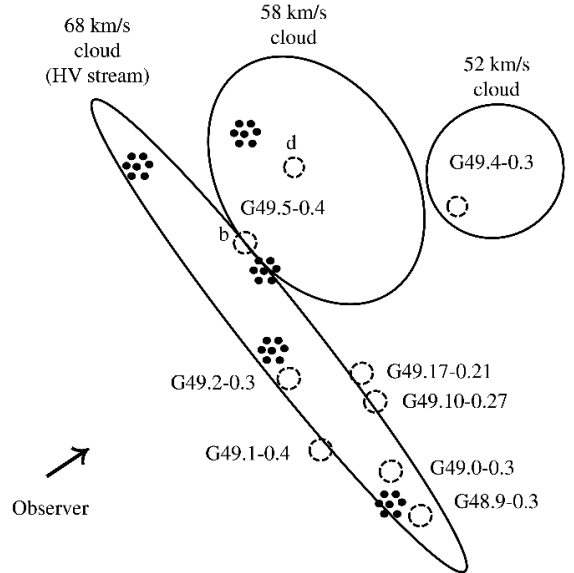


FIG. 29.— Schematic diagram of the W51 H II regions, YSO clusters, and molecular clouds (compare with the diagram in Goudis & Hippelein (1982)). Dashed circles and filled dots represent the H II regions and YSO clusters, respectively.

Scoville et al. (1986) suggested that most high-mass OB stars are formed by cloud-cloud collisions based on the observational evidence for many GMCs associated with H II regions. The studies of star formation triggered by cloud-cloud collisions have been reported in other regions, e.g., NGC 1333 (Loren 1976), DR 21-W75 (Dickel et al. 1978), W49N (Serabyn et al. 1993), and Sagittarius B2 (Hasegawa et al. 1994; Mehringer et al. 1993). The possibility of triggered star formation

by cloud-cloud collisions in W51 has already been suggested (Pankonin et al. 1979; Arnal & Goss 1985; Carpenter & Sanders 1998).

Cloud-cloud collisions may compress the interface region between two colliding clouds and result in the initiation of star formation. The molecular clouds at this interface are heated, but the molecular clouds on the trailing side remain cold. As a result, self-absorption of CO lines is observed toward the interface of cloud-cloud collisions. Models for collisions between two different clouds have shown that a large cloud can be disrupted by the bow shock induced by the collision with a small cloud, but the small cloud is compressed by the shock, and then the post-shock gas of the small cloud can form a new star (Habe & Ohta 1992).

In Figures 26–28, the velocity of 61 km s^{-1} divides the HV stream from the W51 main components. The HV components are related to the streaming motions in the Sagittarius spiral arm. Their elongated structure may result from the associated spiral-wave shock. We agree with earlier suggestions that active massive star formation in the W51 H II region complex is due to a collision between the molecular clouds in the HV stream and the molecular cloud below 61 km s^{-1} (Pankonin et al. 1979; Arnal & Goss 1985; Carpenter & Sanders 1998). In the regions G49.17-0.21 and G49.5-0.4, the self-absorption of $^{12}\text{CO } J = 2 - 1$ occurs around 65 km s^{-1} , coincident with the dark shadow region in IRAC images. In addition, several YSOs are detected inside the low ratio regions ($^{12/13}R_{2-1} < 1.5$). Dark filamentary structures in IR bands (IRDCs) are believed to indicate the earliest stages of massive star-forming regions (Beuther et al. 2007). The IRDCs associated with G49.17-0.21 and G49.5-0.4 have kinematics revealed by the CO maps that appear to be consistent with the cloud collision model for massive star formation.

Star formation in the W51 complex appears to have occurred in a long and large filament along with the H II regions (Figure 1). We could not find clear evidence for a time sequence in this formation process from our data. YSOs along the filament, however, are younger and more massive than those in the surrounding region (see Kang et al. 2009b, Figures 6 and 7).

4.3. Star Formation Efficiency and Rate

Estimating the masses of stars and their parent molecular clouds is important in understanding how molecular clouds evolve and form stars. The star formation efficiency (SFE) is defined as $SFE = M_*/(M_{\text{gas}} + M_*)$, where M_{gas} is the mass of cloud and M_* is the mass of stars in the current generation. Williams & McKee (1997) have found that 10% of the mass of a GMC is converted to stars. Koo (1999) reported SFE values of 7% and 15% in the northwest and southeast components of W51B.

We can compare the gas mass with the mass currently identified as YSOs. We predict that the extended total YSO mass of W51 (W51A + W51B) is $2.1 \times 10^3 M_\odot$ using the mass functions from Kang et al. (2009b) by extrapolating the fitted power laws down to $1 M_\odot$. Total masses of YSOs in W51A and W51B are $0.9 \times 10^3 M_\odot$ and $1.2 \times 10^3 M_\odot$, respectively. As discussed in Section 3.3 we used the LVG formalism for radiative transfer of

CO lines in molecular clouds to estimate the gas mass. Total gas masses of each region are listed in Table 1. The current YSO mass fractions in W51A and W51B are 0.7% and 1.1 %, respectively.

These estimates are for the mass of YSOs *currently* detected in the selected region by extrapolating in mass over our mass function to undetected YSOs. The overall star formation efficiency is the ratio of the mass of stars formed over the cloud lifetime (T_{cloud}) to the initial cloud mass, or approximately, to the current cloud mass plus the mass of all stars formed up to now. We find that only about 1% of the cloud mass is currently in YSOs. We assume the mean timescale for a YSO in the selected mass range to be detected by IRAC (T_{YSO}) is $\sim 3 \times 10^4 \text{ yr}$, which is the statistical lifetime of high-mass protostars in the Cygnus X molecular cloud complex (Motte et al. 2007). If the final star formation efficiency is more like 10% (Williams & McKee 1997; Koo 1999) the star formation process must continue for about $10 \times T_{\text{YSO}}$ at the present rate to convert 10% of the cloud to stars. So the current fraction of YSOs, together with an assumed YSO timescale implies the overall time during which the cloud is actively forming stars. If the YSO timescale for high mass stars is so short, $3 \times 10^4 \text{ yr}$, for a typical cloud lifetime of $3 \times 10^6 \text{ yr}$ and star formation occurred at the presently observed rate, the W51 clouds would convert 10% of their mass to stars in only 1/10th of the cloud lifetime. We are probably observing these clouds at an exceptionally high star formation rate, relative to the average over the cloud lifetime, which typically does not exceed 5 – 10 Myrs (Leisawitz et al. 1989). That is consistent with the remarkably high content of massive YSOs that we found in Kang et al. (2009b). This “burst of star formation” may be a consequence of the passage of the W51 GMC through the spiral arm.

5. SUMMARY

We observed the molecular clouds associated with the active star-forming complex W51 in the ^{12}CO and $^{13}\text{CO } J = 2 - 1$ lines with the HHT. We summarize our results, combining the new CO data of high sensitivity and resolution, together with *Spitzer* 3.6 – 24 μm data:

1. CO emission in the $1^\circ 25' \times 1^\circ 00'$ area divides into three velocity-components, 30 – 55, 56 – 65, and 66 – 85 km s^{-1} . G49.4-0.3 and some clouds in the northwestern part of the map are associated with the lower velocity (30 – 55 km s^{-1}) component. The main molecular clouds in the velocity range of 56 to 65 km s^{-1} are distributed widely throughout the whole region. The higher velocity component ($> 66 \text{ km s}^{-1}$) shows an elongated filamentary structure from southeast to northwest.

2. The average ratios of $^{13}R_{2-1/1-0}$ and $^{13/12}R_{2-1}$ of all H II regions are greater than the values outside the active star-forming regions, which implies that the molecular gas directly associated with the H II regions is dense and highly excited.

3. We compare our CO maps with *Spitzer* data. Strong PAH emission near H II regions seen in IRAC bands coincides with bright CO emission, suggesting that those molecular clouds are associated with the H II regions. Many YSOs are detected in the dark parts near the H II regions on IRAC images.

4. We argue that triggered star formation resulted from H II region expansion into clouds in the shell struc-

ture near W51A and in the region around G49.0-0.3 and G48.9-0.3. We also present evidence of star formation triggered by cloud-cloud collisions in G49.5-0.4 and G49.17-0.21.

5. We estimate the total gas masses of the various interesting regions using an LVG analysis of ^{12}CO and ^{13}CO $J = 2 - 1$ data. By comparing the total gas mass to total mass of YSOs in W51A and W51B, we find current YSO formation efficiencies of 0.7% and 1.1%, respectively, within a timescale of 3×10^4 yr during which massive stars ($> 5M_{\odot}$) would be detected as YSOs. The *current* rate of star formation in the W51 GMC should then be an order of magnitude higher than the rate averaged over an assumed cloud lifetime of 3×10^6 yr, in order to convert 10% of the cloud mass to stars.

We thank Bon-Chul Koo for providing 21 cm radio

continuum data. This research was supported in part by NSF grant AST-0708131 to the University of Arizona, and by the Korea Research Foundation Grant funded by the Korean Government (MOEHRD: KRF-2007-612C00050). MC was supported by the International Research & Development Program of the National Research Foundation of Korea (NRF) funded by the Ministry of Education, Science and Technology (MEST) of Korea (Grant number: K20901001400-09B1300-03210, FY 2009). This publication makes use of molecular line data from the Boston University-FCRAO Galactic Ring Survey (GRS), which is a joint project of Boston University and Five College Radio Astronomy Observatory, funded by the National Science Foundation under grants AST-9800334, AST-0098562, & AST-0100793.

REFERENCES

- Arnal, E. M., & Goss, W. M. 1985, *A&A*, 145, 369
 Benjamin, R. A., et al. 2003, *PASP*, 115, 953
 Beuther, H., Churchwell, E. B., McKee, C. F., & Tan, J. C. 2007, in *Protostars and Planets V*, ed. B. Reipurth, D. Jewitt, & K. Keil (Tucson, AZ: Univ. Arizona Press), 165
 Bieging, J. 1975, in “H II regions and related topics”, eds. T.L. Wilson & D. Downes, *Lecture Notes in Physics*, Vol. 42 (Berlin: Springer), p. 443
 Bieging, J. H., Peters, W. L., Vila Vilaro, B., Schlottman, K., & Kulesa, C. 2009, *AJ*, 138, 975
 Black, J. H., & van Dishoeck, E. F. 1987, *ApJ*, 322, 412
 Brand, J., & Blitz, L. 1993, *A&A*, 275, 67
 Bohlin, R. C., Savage, B. D., & Drake, J. F. 1978, *ApJ*, 224, 132
 Burton, W. B. 1970, *A&AS*, 2, 291
 Cardelli, J. A., Meyer, D. M., Jura, M., & Savage, B. D. 1996, *ApJ*, 467, 334
 Carey, S. J., et al. 2005, *Bulletin of the American Astronomical Society*, 37, 1252
 Carpenter, J. M., & Sanders, D. B. 1998, *AJ*, 116, 1856
 Clark, J. S., & Porter, J. M. 2004, *A&A*, 427, 839
 Crampton, D., Georgelin, Y. M., & Georgelin, Y. P. 1978, *A&A*, 66, 1
 Cyganowski, C. J., et al. 2008, *AJ*, 136, 2391
 Davis, C. J., Kumar, M. S. N., Sandell, G., Froebrich, D., Smith, M. D., & Currie, M. J. 2007, *MNRAS*, 374, 29
 Dickel, J. R., Dickel, H. R., & Wilson, W. J. 1978, *ApJ*, 223, 840
 Downes, D., Wilson, T. L., Bieging, J., & Wink, J. 1980, *A&AS*, 40, 379
 Elmegreen, B. G., & Lada, C. J. 1977, *ApJ*, 214, 725
 Elmegreen, B. G. 1998, *Origins*, ed. C. E. Woodward, J. M. Shull, & H. A. Thronson, Jr. (San Francisco, CA: ASP), 150
 Fazio, G. G., et al. 2004, *ApJS*, 154, 10
 Figuerêdo, E., Blum, R. D., Damineli, A., Conti, P. S., & Barbosa, C. L. 2008, *AJ*, 136, 221
 Fomalont, E. B., & Welachew, L. 1973, *ApJ*, 181, 781
 Genzel, R., & Downes, D. 1977, *A&AS*, 30, 145
 Genzel, R., et al. 1981, *ApJ*, 247, 1039
 Goss, W. M., & Shaver, P. A. 1970, *Australian Journal of Physics Astrophysical Supplement*, 14, 1
 Goudis, C., & Hippelein, H. 1982, *A&A*, 105, 329
 Gritschneider, M., Naab, T., Walch, S., Burkert, A., & Heitsch, F. 2009, *ApJ*, 694, L26
 Habe, A., & Ohta, K. 1992, *PASJ*, 44, 203
 Hasegawa, T., Sato, F., Whiteoak, J. B., & Miyawaki, R. 1994, *ApJ*, 429, L77
 Imai, H., Watanabe, T., Omodaka, T., Nishio, M., Kameya, O., Miyaji, T., & Nakajima, J. 2002, *PASJ*, 54, 741
 Israel, F. P. 1978, *A&A*, 70, 769
 Jackson, J. M., et al. 2006, *ApJS*, 163, 145
 Kang, M., Bieging, J. H., Kulesa, C. A., & Lee, Y. 2009a, *ApJ*, 701, 454
 Kang, M., Bieging, J. H., Povich, M. S., & Lee, Y. 2009b, *ApJ*, 706, 83
 Klein, R. I., Whitaker, R. W., & Sandford, M. T., II 1985, *Protostars and Planets II*, 340
 Koo, B.-C., & Moon, D.-S. 1997, *ApJ*, 475, 194
 Koo, B.-C. 1997, *ApJS*, 108, 489
 Koo, B.-C. 1999, *ApJ*, 518, 760
 Kulesa, C. A., Hungerford, A. L., Walker, C. K., Zhang, X., & Lane, A. P. 2005, *ApJ*, 625, 194
 Kumar, M. S. N., Kamath, U. S., & Davis, C. J. 2004, *MNRAS*, 353, 1025
 Kundu, M. R., & Velusamy, T. 1967, *Annales d'Astrophysique*, 30, 59
 Kutner, M. L., & Ulich, B. L. 1981, *ApJ*, 250, 341
 Leisawitz, D., Bash, F. N., & Thaddeus, P. 1989, *ApJS*, 70, 731
 Loren, R. B. 1976, *ApJ*, 209, 466
 Mehringer, D. M., Palmer, P., Goss, W. M., & Yusef-Zadeh, F. 1993, *ApJ*, 412, 684
 Mehringer, D. M. 1994, *ApJS*, 91, 713
 Moon, D.-S., & Park, Y.-S. 1998, *MNRAS*, 296, 863
 Motte, F., Bontemps, S., Schilke, P., Schneider, N., Menten, K. M., & Brogière, D. 2007, *A&A*, 476, 1243
 Mufson, S. L., & Liszt, H. S. 1979, *ApJ*, 232, 451
 Pankonin, V., Payne, H. E., & Terzian, Y. 1979, *A&A*, 75, 365
 Penzias, A. A., Solomon, P. M., Wilson, R. W., & Jefferts, K. B. 1971, *ApJ*, 168, L53
 Povich, M. S., et al. 2009, *ApJ*, 696, 1278
 Rieke, G. H., et al. 2004, *ApJS*, 154, 25
 Robitaille, T. P., Whitney, B. A., Indebetouw, R., & Wood, K. 2007, *ApJS*, 169, 328
 Russeil, D. 2003, *A&A*, 397, 133
 Sakamoto, S., Hasegawa, T., Handa, T., Hayashi, M., & Oka, T. 1997, *ApJ*, 486, 276
 Sanders, D. B., Clemens, D. P., Scoville, N. Z., & Solomon, P. M. 1986, *ApJS*, 60, 1
 Sault, R. J., Teuben, P. J., & Wright, M. C. H. 1995, in *ASP Conf. Ser. 77, Astronomical Data Analysis Software and Systems IV*, ed. R. A. Shaw, H. E. Payne, & J. J. E. Hayes (San Francisco, CA: ASP), 433
 Schneps, M. H., Lane, A. P., Downes, D., Moran, J. M., Genzel, R., & Reid, M. J. 1981, *ApJ*, 249, 124
 Scoville, N. Z., Sanders, D. B., & Clemens, D. P. 1986, *ApJ*, 310, L77
 Serabyn, E., Guesten, R., & Schulz, A. 1993, *ApJ*, 413, 571
 Shepherd, D. S., et al. 2007, *ApJ*, 669, 464
 Skrutskie, M. F., et al. 2006, *AJ*, 131, 1163
 Smith, H. A., Hora, J. L., Marengo, M., & Pipher, J. L. 2006, *ApJ*, 645, 1264
 Snyder, L. E., & Buhl, D. 1971, *ApJ*, 163, L47
 Subrahmanyan, R., & Goss, W. M. 1995, *MNRAS*, 275, 755
 van Dishoeck, E. F., & Black, J. H. 1988, *ApJ*, 334, 771
 van Gorkom, J. H., Goss, W. M., Shaver, P. A., Schwarz, U. J., & Harten, R. H. 1980, *A&A*, 89, 150
 Walborn, N. R., Maíz-Apellániz, J., & Barbá, R. H. 2002, *AJ*, 124, 1601

- Williams, J. P., & McKee, C. F. 1997, *ApJ*, 476, 166
- Wilson, T. L., Mezger, P. G., Gardner, F. F., & Milne, D. K. 1970, *Astrophys. Lett.*, 5, 99
- Wynn-Williams, C. G., Becklin, E. E., & Neugebauer, G. 1974, *ApJ*, 187, 473
- Xu, Y., Reid, M. J., Menten, K. M., Brunthaler, A., Zheng, X. W., & Moscadelli, L. 2009, *ApJ*, 693, 413